

THE REST-FRAME OPTICAL SPECTRA OF SCUBA GALAXIES

A. M. SWINBANK,¹ IAN SMAIL,¹ S. C. CHAPMAN,² A. W. BLAIN,² R. J. IVISON^{3,4} & W. C. KEEL⁵

Version: September 15, 2018 Received 2004 07 24; Accepted: 2004 08 17

ABSTRACT

We present near-infrared spectroscopy and narrow-band imaging at the wavelength of redshifted H α for a sample of 30 high-redshift, far-infrared luminous galaxies. This sample is selected from surveys in the sub-millimeter, millimeter and radio wavebands and has complete redshift coverage with a median redshift of $z \sim 2.4$. We use our data to measure the H α properties of these systems and to gauge the prevalence of active galactic nuclei (AGN) in these galaxies through their [NII]/H α ratios and H α line widths. Removing obvious AGN, we find that the predicted H α star formation rates in this diverse population are suppressed (by a factor of ~ 10) compared to those derived from their far-infrared luminosities. Using the AGN indicators provided by our near-infrared spectra, we estimate that AGN are present in at least 40% of the galaxies in our sample. To further investigate this, we construct a composite rest-frame spectrum for both the entire sample and for those galaxies which individually show no signs of nuclear activity. We find [NII]/H α ratios for both composite spectra which suggest that the energy output of the galaxies is star-formation- rather than AGN-dominated. However, we also find that the H α line in the composite non-AGN spectrum is best fit with an underlying broad-line component with a narrow/broad flux ratio of 0.45 ± 0.20 . The median H α line width for our sample (removing obvious AGN) is $400 \pm 70 \text{ km s}^{-1}$ (FWHM), and the typical spatial extent of the H α emission in our narrow-band observations is $\lesssim 4\text{--}8 \text{ kpc}$, which indicates a dynamical mass of $1\text{--}2 \times 10^{11} M_{\odot}$ with corresponding dynamical times of $10\text{--}20 \text{ Myr}$. Using both high-resolution imaging and spectroscopically identified velocity offsets, we find that seven of the far-infrared luminous galaxies have companions, suggesting that they are undergoing interactions/mergers and from their relative velocities we can determine a dynamical mass of $1.5 \pm 0.9 \times 10^{11} M_{\odot}$. These measurements are comparable to millimeter CO estimates for the dynamical masses of these systems on similar scales, and larger than recent estimates of the dynamical masses of UV-selected galaxies at similar redshifts derived in an identical manner. Using the [NII]/H α index to predict abundances, we investigate the Luminosity–Metallicity relation for these galaxies and find that many have metallicities consistent with UV-selected high-redshift galaxies and slightly lower than local luminous infrared and elliptical galaxies (although we caution that our metallicity estimates have possible systematic uncertainties). We also compared our H α and far-infrared luminosities with deep *Chandra* observations of a subset of our survey fields and use these data to further assess their AGN content. We conclude that these high-redshift, far-infrared luminous galaxies represent a population of massive, metal-rich, merging systems with high instantaneous star formation rates, strong dust obscuration and actively-fueled AGN which are likely to be the progenitors of massive local elliptical galaxies.

Subject headings: galaxies: active — galaxies: evolution — galaxies: high-redshift — galaxies: starburst — submillileter

1. INTRODUCTION

Recent surveys in the submillimeter (sub-mm), millimeter (mm) and radio wave bands suggest that the star formation density detectable by these dust-independent tracers has evolved strongly with redshift. Indeed, this evolution appears to outstrip that found using tracers which are more sensitive to dust obscuration, suggesting that an increasing proportion of activity in more distant galaxies may be highly obscured (Blain et al. 1999b). The populations resolved in these wavebands appear to be responsible for much of the energy density in the extragalactic far-infrared/sub-mm background (Smail et al. 2002; Cowie et al. 2002; Chapman et al. 2004a). However, the extreme faintness of optical counterparts to these obscured galaxies has made it very difficult to obtain accurate redshifts and measure intrinsic properties (e.g., Simpson et al. 2004).

The best-studied examples of the high-redshift, far-infrared

luminous galaxy population are those identified in the sub-mm wave band using the SCUBA camera on the JCMT. The median redshift for this population is $\langle z \rangle \sim 2.4$ (Chapman et al. 2003a, 2003b, 2004a), and their sub-mm fluxes suggest that they have bolometric luminosities $> 10^{12} L_{\odot}$ – implying that they are Ultraluminous Infrared Galaxies (ULIRGs). The nature of this population and their relevance to models of galaxy formation models and evolution are particularly important (e.g., Genzel et al. 2003; Baugh et al. 2004). If they are powered purely by star-formation then these galaxies form about half of the stars seen locally (Lilly et al. 1999). However, both AGN activity and star-formation could contribute to their immense far-infrared luminosities, and without further information it is impossible to disentangle the precise energy source (Alexander et al. 2003a).

Rest-frame optical emission line properties provide a pow-

¹Institute for Computational Cosmology, Department of Physics, University of Durham, South Road, Durham DH1 3LE, UK – Email: a.m.swinbank@dur.ac.uk

²Astronomy Department, California Institute of Technology, 105-24, Pasadena, CA 91125, USA

³Astronomy Technology Centre, Royal Observatory, Blackford Hill, Edinburgh, EH19 3HJ, UK

⁴Institute for Astronomy, University of Edinburgh, Edinburgh, EH19 3HJ, UK

⁵Department of Physics and Astronomy, University of Alabama, Tuscaloosa, AL 35487, USA

erful tool to investigate star formation rates (SFRs), power sources, and metallicity of galaxies. In particular, the Hydrogen Balmer emission line series is one of the primary diagnostics of the SFR in nearby galaxies, with the strength of $H\alpha$ and its relative insensitivity to extinction making it the line of choice. The nebular recombination lines are a direct probe of the young, massive stellar population, since only stars with masses $\gtrsim 10M_{\odot}$ and lifetimes $\lesssim 20$ Myr contribute significantly to the integrated ionising flux. Hence, the strength of these emission lines provides a nearly instantaneous measure of the SFR, independent of the previous star formation history. Moreover, by combining the SFR inferred from this diagnostic line with the far-infrared emission (which comes from reprocessed radiation which has been absorbed and re-emitted by dust in the far-infrared at wavelengths of 10–300 μm), we can gauge the prevalence of dust obscuration. The width of the $H\alpha$ line and its intensity relative to other rest-frame optical lines can also give important information about the presence and luminosity of an AGN within a galaxy (Veilleux et al. 1987, 1995).

$H\alpha$ is visible in the near-infrared wave band out to $z \sim 2.6$ and projects exploiting the $H\alpha$ emission at these high redshifts have provided unique insights into the star formation properties of distant galaxies (e.g., Yan et al. 1999; Erb et al. 2003; Shapley et al. 2004; van Dokkum et al. 2004). With precise redshifts for the far-infrared luminous population from the work of Chapman et al. (2004a, 2004b), we can efficiently target the $H\alpha$ emission from the galaxies to understand the formation and evolution of this population and can identify the power sources, star formation rates, metallicities (which are accessible through the $[\text{NII}]/H\alpha$ $[\text{N2}]$ index; Pettini & Pagel 2004), and masses, as well as more general issues such as their relation to other classes of high-redshift sources such as Lyman Break Galaxies (LBGs; Pettini et al. 2001; Erb et al. 2003; Shapley et al. 2004).

As well as measuring the star formation rate from $H\alpha$, it is also possible to measure dynamics of these systems from the same spectra. Far-infrared luminous galaxies at $z \sim 2$ appear morphologically complex (Chapman et al. 2003b; Smail et al. 2004). By measuring the internal dynamics of the galaxies or the velocity offsets between companions, we can also place limits on their masses and so test if these galaxies are truly massive systems (Genzel et al. 2003).

In this paper we present the results from a near-infrared study of a sample of far-infrared- detected galaxies at $z=1.4$ – 2.7 . We use the $H\alpha$ emission line to derive their star formation rates and dynamics. We investigate the metallicity of these galaxies through their $[\text{NII}]/H\alpha$ emission and dynamics as traced by velocity structures visible in $H\alpha$ emission in a subset of galaxies. Using *Chandra* data, we also compare our $H\alpha$ and far-infrared luminosities with X-ray luminosities in several of our survey fields.

In §2 we present the data reduction and results from the spectroscopic survey and narrow-band imaging. In §3 we discuss the $H\alpha$ properties of the far-infrared luminous galaxies and present a discussion of the star formation rates estimated from their $H\alpha$ and far-infrared emission and of their dynamics, metallicities, and X-ray counterparts. We present our conclusions in §4. We use a cosmology with $H_0 = 72 \text{ km s}^{-1}$, $\Omega_0 = 0.3$ and $\Lambda_0 = 0.7$ in which $1''$ corresponds to 8.2 kpc at $z = 2.4$.

2. OBSERVATIONS AND ANALYSIS

Our target sample comes from two catalogs of far-infrared luminous galaxies by Chapman et al. (2003a, 2004a). The majority of our sample comprises sub-mm detected, radio-identified galaxies (SMGs). These galaxies have precise positions from the microjansky (μJy) radio emission and are confirmed to be far-infrared luminous from their detection in the sub-mm/mm wavebands with SCUBA or MAMBO. The radio-detected subset of the SMG population represents $\sim 60\%$ – 70% of all SMGs brighter than $\gtrsim 5 \text{ mJy}$ (Ivison et al. 2002; Chapman et al. 2001; Wang et al. 2004). In addition, we have also included a small number of optical and sub-mm faint radio galaxies (OFRGs) at similar redshifts which have been proposed to be similarly luminous far-infrared galaxies, but with somewhat hotter dust temperatures resulting in them having comparatively faint submm fluxes (Chapman et al. 2004b; Blain et al. 2004). The median redshift of the combined sample is $\langle z \rangle = 2.4 \pm 0.2$. For the purposes of this study we chose targets whose redshifts place $H\alpha$ in spectral regions which are relatively free from strong atmospheric absorption and emission.

We have explored two routes to investigate the $H\alpha$ emission from SMGs/OFRGs. First, we used narrow-band imaging to assess the $H\alpha$ fluxes of galaxies in our sample – from both a tunable filter (NSFCAM on IRTF) and more traditional narrow-band filters (with the UFTI near-infrared imager on UKIRT) for galaxies whose redshifts serendipitously place $H\alpha$ in the filter bandwidth. These narrow-band observations provide the opportunity to determine the total $H\alpha$ emission from the SMGs/OFRGs and search for any extended emission or spatial companions.

Second, we used classical long-slit near-infrared spectroscopy with the NIRSPEC spectrograph on Keck and the ISAAC spectrograph on the VLT. These observations allow us to measure precise systemic redshifts for these SMGs/OFRGs, with much higher reliability than that available from their rest-frame UV emission – which frequently show velocity shifts of 100's of km s^{-1} . These precise redshifts are necessary for interferometric CO follow-up of these galaxies (Neri et al. 2003; Greve et al. 2004). The long-slit spectroscopic observations also allow us to measure the $H\alpha$ luminosities and SFR($H\alpha$) and to gauge the prevalence of AGN in these galaxies – through the detection of broad lines and extreme $[\text{NII}]/H\alpha$ flux ratios.

These two approaches therefore provide complimentary information on the $H\alpha$ emission properties of the SMG/OFRG population.

2.1. Narrow-band Imaging

2.1.1. IRTF

Narrow-band imaging of five targets was carried out using the NASA Infra-Red Telescope Facility⁵(IRTF) 3-m Telescope between 2003 April 28 and May 02. The observations were made in generally photometric conditions and $\sim 1''$ seeing. We used the NSFCAM camera (Shure et al. 1993) which employs a 256×256 InSb detector at $0.15'' \text{ pixel}^{-1}$ to give a $38''$ field of view (which probes roughly 300 kpc at $z \sim 2.4$). The continuously variable tunable narrow-band filter (CVF) in NSFCAM provides an $R = 90$ passband which was tuned to the galaxy redshifts measured from the UV spectra from Chapman et al. (2003a, 2004). Shorter, matched broad-band imaging was interspersed between the narrow-band exposures to provide continuum subtraction.

⁵The Infrared Telescope Facility is operated by the University of Hawaii under Cooperative Agreement no. NCC 5-538 with the National Aeronautics and Space Administration, Office of Space Science, Planetary Astronomy Program.

The observations were taken in a standard nine-point dither pattern and reduced using a running flat field of the six nearest temporally adjacent frames, masking bright objects before creating the flat-field frame. The final image was made by averaging the flat-fielded frames with a 3σ clip to reject cosmic rays. To calibrate our data, we observed UKIRT faint photometric standards (Hawarden et al. 2001). These standards were observed at similar air masses and using the same instrumental configuration as the target galaxies. As well as providing good flux calibrations, these observations also allow us to calculate the relative throughput of the narrow-band and broad-band filters. This allows precise subtraction of the continuum contribution from the $H\alpha$ emission in the narrow-band filter. The NS-FCAM CVF filter is wide enough that it contains both the $H\alpha$ and [NII] emission lines (with the [NII] emission line included at 95% of peak transmission assuming that $H\alpha$ falls at the peak of the filter trace). The median [NII]/ $H\alpha$ ratio in our spectroscopic sample is 0.25, and we therefore apply a 24% correction to the narrow-band flux to account for the [NII] emission line. Exposure times, central wavelengths, and measured $H\alpha$ fluxes from these observations are given in Tables 1 & 2. We illustrate the $H\alpha$ morphology for one of the more unusual galaxies in our sample in Fig. 4 and discuss this in more detail in §3.1

2.1.2. UFTI

We obtained classical narrow-band imaging of two SMGs, SMMJ105226.61 and SMMJ131232.31, whose redshifts should place $H\alpha$ emission in the Br γ and H $_2$ S1 filters, respectively. These data were taken with the UFTI near-infrared camera (Roche et al. 2003) on UKIRT⁶ on 2003 February 25–27 in $\lesssim 0.7''$ seeing and photometric conditions. The UFTI camera has a 1024×1024 HgCdTe array and a plate scale of $0.091'' \text{ pixel}^{-1}$, giving a field of view of $92'' \times 92''$ (which probes roughly 0.75 Mpc in our adopted cosmology). To provide continuum subtraction, we interspersed the narrow-band observations with K -band imaging. The data were reduced using the ORAC-DR pipeline. The relative throughputs of the broadband and narrowband filters and flux calibration were determined using Two Micron All Sky Survey (2MASS) K -band photometry on bright ($K \sim 12$) stars within the $92''$ field of view.

TABLE 1: SUMMARY OF NARROW BAND IMAGING

| Object | λ_{cen} (μm) | t_{exp} (ks) | |
|-------------------------|---|-----------------------|-----------|
| | | K | $H\alpha$ |
| IRTF Tunable Filter | | | |
| SMMJ105230.73+572209.5 | 2.3692 | 2.5 | 12.6 |
| SMMJ123635.59+621424.1 | 1.9721 | 1.4 | 9.0 |
| SMMJ131215.27+423900.93 | 2.3396 | 1.4 | 7.2 |
| SMMJ140104.96+025223.5 | 2.3396 | 0.7 | 9.0 |
| SMMJ163631.47+405556.9 | 2.1544 | 4.5 | 14.4 |
| UKIRT Narrow-band | | | |
| SMMJ105226.61+572113.0 | 2.248 | 5.6 | 22.7 |
| SMMJ131232.31+423949.5 | 2.166 | 4.0 | 15.0 |

Notes: λ_{cen} denotes the central position of the narrow-band filter for the observations.

All of our narrow-band observations were taken based on the rest-frame UV redshifts and assuming that the rest-frame optical redshifts were in agreement. However, a velocity offset of

$\sim 500 \text{ km s}^{-1}$ between the rest-frame UV and optical emission lines can redshift the $H\alpha$ out of the narrow-band filter. Shifts of the amplitude are relatively rare, and so we assume that our observations have sampled the bulk of the $H\alpha$ emission in these galaxies.

2.2. Keck Spectroscopy

We obtained near-infrared spectra of 24 SMGs/OFRGs using NIRSPEC (McLean et al. 1998) on the 10-m Keck telescope.⁷ These observations were obtained on the nights of 2003 August 3, in non-photometric conditions; in somewhat better conditions on 2004 February 1; in $0.5''$ seeing and in photometric condition between 2004 April 6–9 and 2004 July 31. In all four instances, observations were made using the low-resolution, longslit mode with a 4-pixel wide ($0.76''$) slit. Spectra were obtained in the K -band using the N7 or K' filters. In this configuration the resolution is $R \sim 1500$. To subtract sky emission, the observations were made in a standard ABBA sequence, where the object is nodded along the slit by 10 – $20''$. The total integration times are listed in Table 2 (the integration times of individual exposures were typically ~ 600 s). One goal of these observations was to provide precise systemic redshifts of the SMGs/OFRGs to compare to those measured in the UV and also to provide a precise redshift for our on-going CO mapping program on the Plateau de Bure interferometer (Neri et al. 2003; Greve et al. 2004). To maximise the sample size, the exposure times were therefore kept short and so the $H\alpha$ lines are rarely detected with sufficient signal-to-noise ratio to measure more than their most basic characteristics. We note that the success rate for detecting $H\alpha$ emission in the SMGs/OFRGs in the near-infrared is $\sim 70\%$. This estimate is based on the results from the third observing run, which was largely photometric since the first two observing runs were plagued by clouds. In cases in which there was no detection of either continuum or $H\alpha$ emission, we have assumed that the target was not on the slit (as a result of an offset error or loss of guiding during the offset from a nearby bright star). In two cases we detected continuum from the target but could not detect any emission lines. In these cases we have quoted upper limits for the $H\alpha$ luminosity and SFR.

The spectroscopic observations were reduced using the WMKONSPEC package in IRAF. We remap the two dimensional spectra using linear interpolation to rectify the spatial and spectral dimensions. After subtracting pairs of nod-positions, residual sky features were removed in IDL using sky regions on either side of the object spectrum. The wavelength calibration from the 2003 run used the night sky lines, while for the 2004 observing runs we used an argon arc lamp. The output pixel scale is $4.3 \text{ \AA pixel}^{-1}$, and the instrumental profile has a FWHM of 15 \AA (measured from the widths of the sky-lines). In all line widths quoted in the following sections we have deconvolved the instrumental profile from the FWHM of the galaxies.

The redshifts of our targets have been relatively well constrained from rest-frame UV spectroscopy carried out with LRIS on the Keck telescope. However, again we stress that the rest-frame UV and optical emission lines can show velocity offsets of a few 100 's km s^{-1} (Pettini et al. 2001; Erb et al. 2003; Shapley et al. 2003; Smail et al. in prep). With knowledge of the UV redshift we were able to identify the $H\alpha$ and [NII] emission in each spectrum and ensure the correct line identification.

⁶The United Kingdom Infrared Telescope is operated by the Joint Astronomy Centre on behalf of the U.K. Particle Physics and Astronomy Research Council.

⁷Obtained at the W.M. Keck Observatory, which is operated as a scientific partnership among the California Institute of Technology, the University of California and the National Aeronautics and Space Administration. The Observatory was made possible by the generous financial support of the W.M. Keck Foundation.

As the first two and final observing runs were non-photometric, we calibrate the integrated $H\alpha$ fluxes onto an absolute flux scale by careful comparison of the spectra with the K -band photometry of the galaxies (Smail et al. 2004). We convolve the galaxy spectra with the normalised K -band filter response curve to obtain the mean flux conversion factor for each galaxy spectrum. We also note that the atmospheric transmission at the wavelength of redshifted $H\alpha$ is ~ 1 for all targets except SMMJ123621.27, where the transmission is 0.75 ± 0.02 . For the third observing run we used a standard star (FS 27) to flux-calibrate the data. We also use the broadband photometry to flux-calibrate these data in order to verify that the process applied to calibrate the previous observations is reliable and obtain a mean ratio of calibration factors of 1.05 ± 0.10 . This gives us confidence that using the photometry to flux-calibrate gives consistent results. All of the objects included here have detectable continuum emission. Where the continuum or emission lines are faint, we binned the reduced two dimensional frames by a factor of two in both the spatial and spectral dimension to improve the contrast prior to extraction. We show the extracted spectra for the whole sample in Fig. 1.

2.3. ISAAC VLT Spectroscopy

During the night of 2003 October 21, observations of SMMJ221733.79 were obtained in queue mode with the ISAAC spectrograph on the VLT⁸ (Moorwood 1997). The data were taken using the medium-resolution ($R = 3000$) grating and a $1''$ slit (with an instrumental FWHM of $\sim 6.7\text{\AA}$) and in $0.8''$ seeing. In this configuration the output pixel scale is 1.2\AA pixel^{-1} . The total integration time was 3.0 ks with the data taken in $4 \times 750\text{s}$ exposures in the standard ABBA sequence where the object is nodded along the slit by $10\text{--}20''$ to achieve sky subtraction. We reduced the data using the ISAAC data-reduction pipeline, which rectifies, flat-fields, and wavelength calibrates the two dimensional frames. Prior to extraction, the data were binned by a factor of two in the spectral direction to boost the contrast of the object. We observed the standard star HIP 032007 for flux calibration. The derived $H\alpha$ fluxes and redshifts are listed in Table 2, and the spectra are shown in Fig. 1.

2.4. Spectral Analysis

To accurately determine the redshift for each galaxy, we fit both the continuum level and emission lines: $H\alpha\lambda 6562.8$ and $[\text{NII}]\lambda\lambda 6548.1, 6583.0$ simultaneously with a flat continuum plus Gaussian profiles using a χ^2 fit and taking into account the greater noise in regions of strong sky emission. As well as fitting the narrow-line $H\alpha$ and $[\text{NII}]$ emission, we also attempt to identify any underlying broad-line $H\alpha$ (AGN) component by fitting a broad Gaussian profile at the same redshift as the narrow-line $H\alpha$ emission but only accepting the result if the χ^2 fit is significantly better (with $>90\%$ confidence limit) than with no broad-line component. This allows us to deconvolve the narrow-line $H\alpha$ flux, which may arise from star-formation, from the broad-line $H\alpha$ flux from an AGN. For the observations which were flux-calibrated using the K -band photometry we estimate the errors in the $H\alpha$ flux and continuum levels using both the uncertainty in the K -band magnitude and the errors on the best fit to the emission line, evaluated by varying the fit by $\Delta\chi^2 = 1$. The error bars on the emission-line fluxes and equivalent widths are therefore conservative errors which take

into account the error in using the K -band photometry and the uncertainty which arises from the signal-to-noise ratio in the data. This flux error is propagated through to the star formation rate. We list the parameters for the fits for narrow (and where relevant broad) components in Table 2, along with their uncertainties. We note that the $[\text{SII}]\lambda\lambda 6716, 6731$ doublet is detected in at least three individual spectra: SMMJ123600.00, SMMJ163650.43, and SMMJ163639.01.

The ratio of $[\text{NII}]$ to $H\alpha$ line fluxes from our spectra, as well as the presence of a broad component, can be used to identify luminous AGN in these galaxies (e.g., Veilleux et al. 1987; Armus et al. 1989). We measure all of these observables from our spectra and use them to flag galaxies whose $H\alpha$ and far-infrared luminosities could be affected by emission from an AGN, rather than being star-formation dominated (Table 2). Using the $[\text{NII}]/H\alpha$ emission line ratio and $H\alpha$ line width as diagnostics, we separate our sample into three classes: AGN dominated, intermediate, and systems whose properties are consistent with star-formation (but may still contain some AGN). In a later section we test the reliability of these classes through the use of deep X-ray observations. We classify galaxies whose near-infrared spectra show $[\text{NII}]/H\alpha < 0.7$ and $\text{FWHM}_{\text{rest}} < 500\text{km s}^{-1}$ as star-bursts (SB). Galaxies with $\text{FWHM}_{\text{rest}}$ between 500 and 1000km s^{-1} are classified as intermediate, while galaxies with $[\text{NII}]/H\alpha > 0.7$ and/or $\text{FWHM}_{\text{rest}} > 1000\text{km s}^{-1}$ are classified as AGN. Using this classification, $\sim 40\%$ (9/24) of the objects in our detected spectroscopic sample have some indication of an AGN (most classifications are based on $H\alpha$ line widths, with only one AGN changing classification if we remove the limits on $[\text{NII}]/H\alpha$). This is similar to the rate estimated from UV spectroscopy and high-resolution radio imaging (Chapman et al. 2003a, 2003b, 2004c). By comparing the rest-frame UV and optical spectral classifications (Table 2), we find that the fifteen galaxies identified as SB in the rest-frame UV are classified as SB[9], AGN[3] and intermediate[3] from their rest-frame optical spectra. Likewise, the three AGN identified in the rest-frame UV are all classified as AGN from their rest-frame optical spectra. We conclude that these classifications are in reasonable agreement. However, we note that their AGN could be easily hidden from view in both wavebands (see e.g., §3.5). Looking at the far-infrared luminosities of the three spectral classes we find median values of $5.2 \pm 3.0 \times 10^{12} L_{\odot}$ for the SMGs/OFRGs classed as AGN, $6.6 \pm 0.7 \times 10^{12} L_{\odot}$ and $5.4 \pm 1.4 \times 10^{12} L_{\odot}$ for the starbursts and intermediate respectively. We thus find no strong evidence for a strong luminosity dependence of the different spectral classes.

To determine total $H\alpha$ fluxes, we have also corrected for slit losses based on the average K -band light distribution of the galaxies. As we know the position, width, and orientation of the spectroscopic aperture for each galaxy, we use the K -band images to calculate the fraction of the total K -band light that enters the spectroscopic aperture. The galaxies are frequently extended and disturbed (e.g., Smail et al. 2004), and while this correction is uncertain, we view it as more reliable to apply this factor before comparing $H\alpha$ to far-infrared star formation rates, rather than to ignore it. However, we note that using a single factor for correcting slit losses may contribute some scatter when comparing the $H\alpha$ and far-infrared star formation rates. By careful comparison of a simulated slit for each galaxy in our sample with the K -band imaging, we estimate the fraction

⁸Based on observations collected with the ESO VLT-UT1 Antu Telescope (072.A-0156)

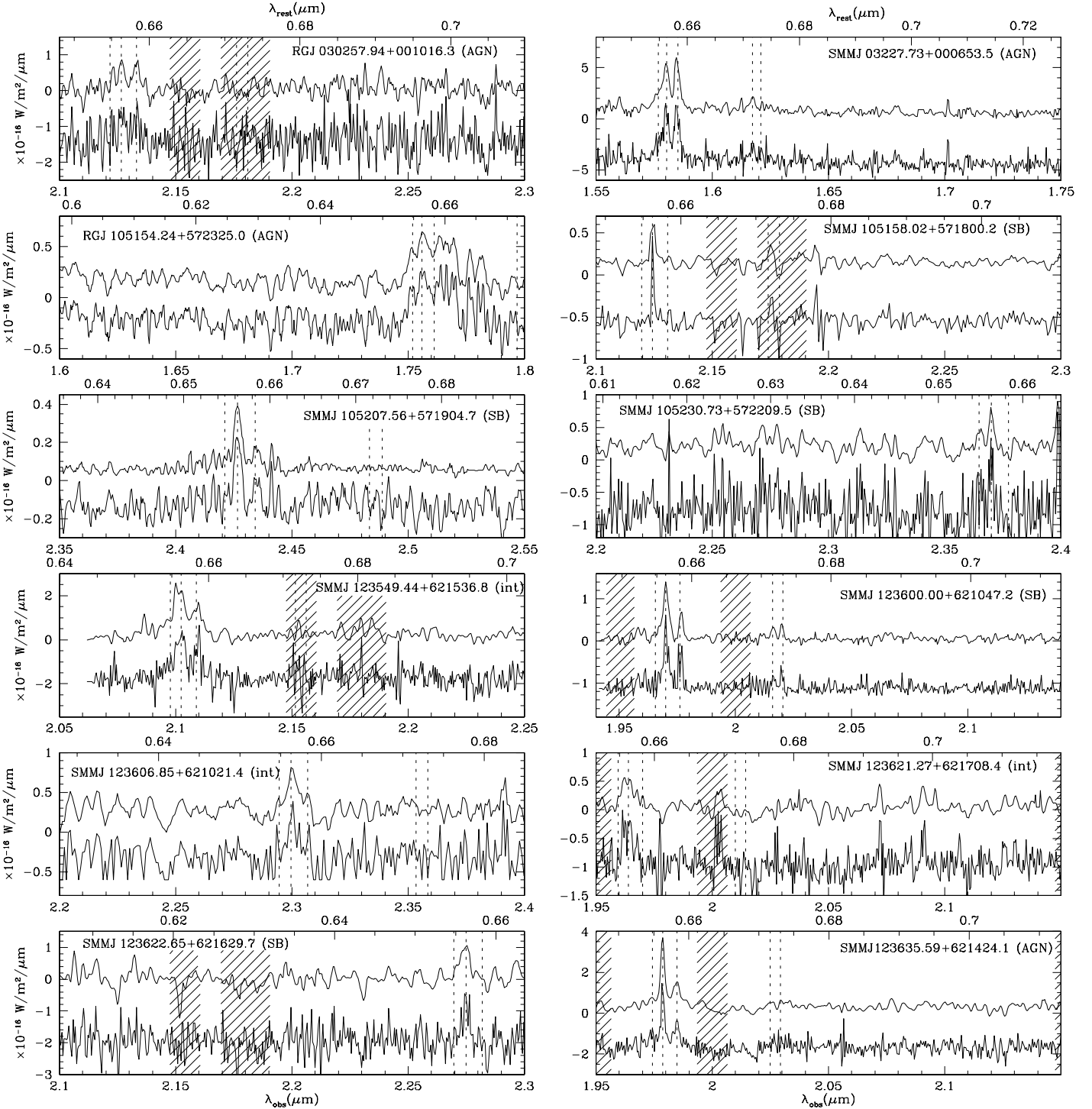
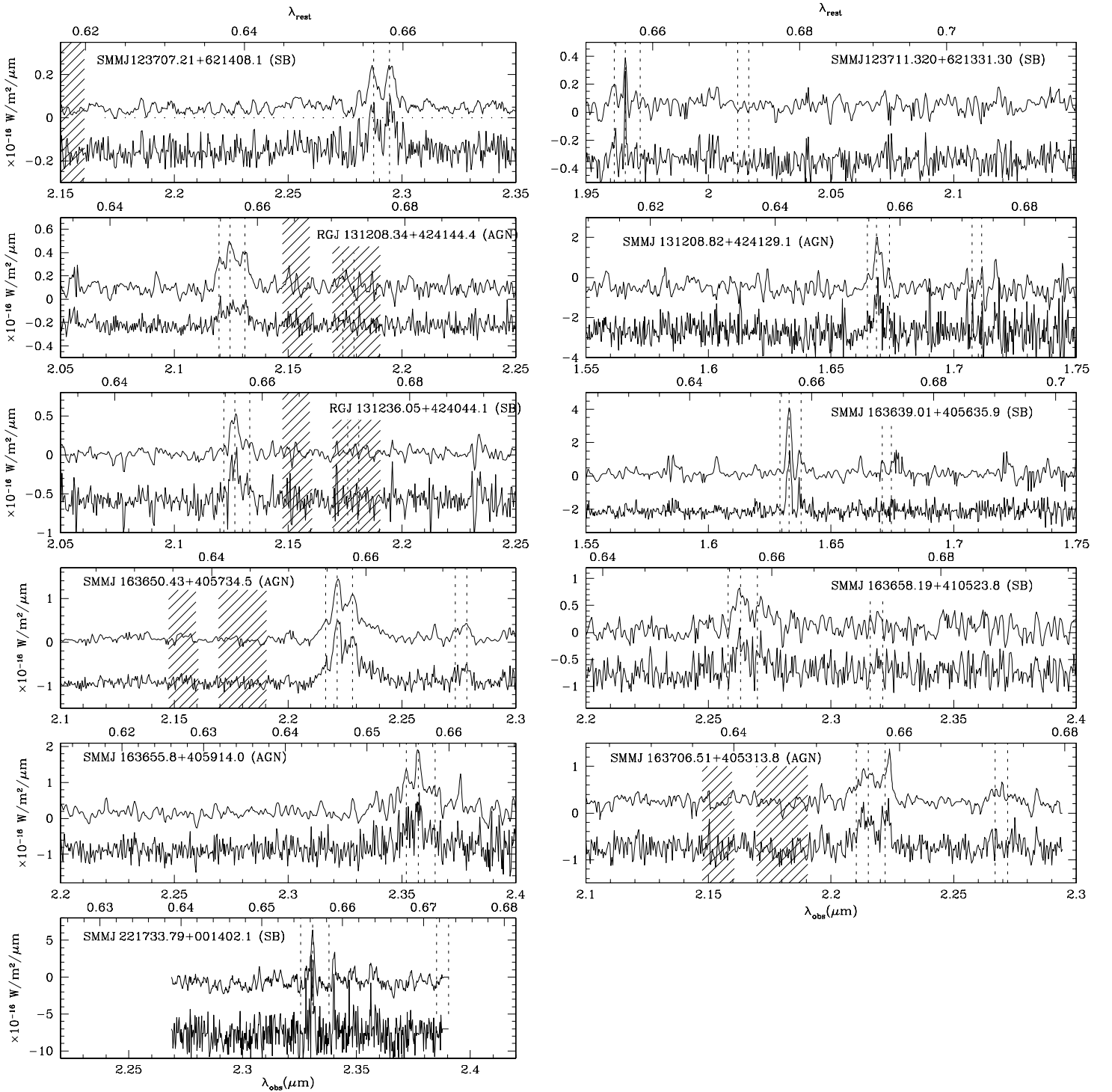


FIG. 1. — $H\alpha$ spectra for the SMGs/OFRGs in our sample. The lower spectrum in each panel is the raw spectrum (offset in flux scale for clarity). The upper spectrum is smoothed to the instrumental resolution. The dashed vertical lines show the positions of the $H\alpha\lambda 6562.8$, $[NII]\lambda\lambda 6548.1, 6583.0$, and $[SII]\lambda\lambda 6717, 6731$, emission lines. The lower axis scale shows the observed wavelength, while the upper scale displays the rest-frame wavelength. The shaded areas are regions of strong sky emission. The spectra are ordered in right ascension range as in Table 2, and we label each galaxy with its spectral classification from §2.4. Note that we identify two $H\alpha$ emission lines from SMMJ123707.21 rather than $H\alpha + [NII]$ (see §3.1). The final spectra are higher resolution ISAAC/VLT spectra (Table 2).

of the flux entering the slit compared to the total K -band flux of the galaxy, f , and obtain a mean value of $f = 0.62 \pm 0.06$. We assume that the equivalent width of the $H\alpha$ emission line is constant across the galaxy and so only those galaxies with spectra taken in photometric conditions, whose flux calibration

was carried out using the standard star observations, require this correction to their $H\alpha$ flux.

Finally, we note that there are two repeated observations of targets between the spectroscopic and narrow-band imaging samples: SMMJ105230.60 and SMMJ123635.59 — as well



as narrow-band imaging of SMMJ140104.96 for which an $H\alpha$ spectrum exists in the literature ($0.56 \pm 0.08 \times 10^{-18} \text{ W m}^{-2}$; Iverson et al. 2000). The agreement between the $H\alpha$ fluxes from the two techniques is very good (Table 2), with a median ratio of spectroscopic to imaging fluxes of 0.96 ± 0.04 . On the basis of this good agreement we feel confident in combining the spectroscopic and narrow-band imaging data to discuss the $H\alpha$ luminosities of SMGs/OFRGs in the following sections.

2.5. Star Formation Rates

For solar abundances and adopting a Salpeter initial mass function (IMF), the conversion between $H\alpha$ flux and SFR is $\text{SFR}(\text{M}_{\odot} \text{ yr}^{-1}) = 7.9 \times 10^{-35} L(\text{H}\alpha) \text{ W}$ (Kennicutt et al. 1998). This calibration assumes that all of the ionising photons are reprocessed into nebular lines (i.e., they are neither absorbed by dust before they can ionise the gas, nor do they escape the galaxy).

TABLE 2: SUMMARY OF RESULTS

| Object | t_{exp} (ks) | z | H α Flux (10^{-19} W m $^{-2}$) | FWHM $_{\text{rest}}$ (km s $^{-1}$) | EW $_{\text{rest}}$ (Å) | SFR(H α) (M_{\odot} yr $^{-1}$) | [NII]/H α | L $_{\text{FIR}}$ (10^{12} L/ L_{\odot}) | Class (UV / H α) |
|----------------------------|--------------------------|------------|---|--|----------------------------|--|------------------|---|-----------------------------|
| Spectroscopy | | | | | | | | | |
| NIRSPEC Keck | | | | | | | | | |
| SMM J030227.73+000653.5 | 3.0 | 1.4076[2] | 15.2 \pm 2.0 | 420 \pm 15 | 85 \pm 10 | 140 \pm 18 | 1.38 \pm 0.07 | 5.78 $^{+2.44}_{-0.82}$ | SB / AGN |
| RGJ 030258.94+001016.3 | 2.0 | 2.2404[8] | 1.8 \pm 0.5 | 327 \pm 22 | 360 \pm 110 | 51 \pm 15 | 1.13 \pm 0.40 | 7.74 $^{+1.41}_{-1.41}$ | int / AGN |
| RGJ 105154.24+572325.0 | 4.8 | 1.681[8] | 2.7 \pm 1.9 | 1565 \pm 250 | 91 \pm 6 | 61 \pm 40 | < 0.2 | 2.80 $^{+0.35}_{-0.35}$ | SB / AGN |
| SMM J105158.02+571800.3 | 2.4 | 2.2390[4] | 2.4 \pm 1.2 | 257 \pm 44 | 21 \pm 5 | 57 \pm 15 | < 0.1 | 10.40 $^{+1.90}_{-1.00}$ | SB / SB |
| SMM J105207.56+571904.7 | 4.8 | 2.692[2] | 1.3 \pm 0.4 | 285 \pm 20 | 21 \pm 4 | 217 \pm 64 | 0.18 \pm 0.10 | 9.46 $^{+2.70}_{-2.70}$ | SB / SB |
| SMM J105230.73+572209.5 | 2.4 | 2.6100[3] | 1.2 \pm 0.3 | 171 \pm 40 | 10 \pm 3 | 42 \pm 15 | < 0.05 | 10.29 $^{+0.75}_{-1.12}$ | SB / SB |
| SMM J123549.44+621536.8 | 2.4 | 2.2032[3] | 15 \pm 1 | 536 \pm 33 | 184 \pm 9 | 239 \pm 18 | 0.50 \pm 0.10 | 6.76 $^{+1.50}_{-1.12}$ | SB / int |
| SMM J123600.15+621047.2 | 1.2 | 2.0017[2] | 3.7 \pm 0.3 | 305 \pm 12 | 91 \pm 8 | 126 \pm 8 | 0.20 \pm 0.10 | 10.50 $^{+1.50}_{-1.50}$ | SB / SB |
| SMM J123606.85+621021.4 | 2.4 | 2.5054[8] | 2.0 \pm 0.3 | 612 \pm 35 | 28 \pm 5 | 78 \pm 12 | < 0.2 | 8.70 $^{+1.80}_{-1.20}$ | SB / int |
| SMM J123621.27+621708.4 | 2.4 | 1.9924[7] | 2.0 \pm 0.6 | 586 \pm 92 | 212 \pm 25 | 56 \pm 16 | 0.20 \pm 0.15 | 12.76 $^{+1.30}_{-2.25}$ | SB / int |
| SMM J123622.65+621629.7 | 2.4 | 2.4662[5] | 3.4 \pm 0.6 | 434 \pm 25 | 137 \pm 40 | 125 \pm 20 | < 0.05 | 9.01 $^{+1.88}_{-2.03}$ | SB / SB |
| SMM J123635.59+621424.1 | 1.8 | 2.0150[2] | 4.2 \pm 0.3 | 240 \pm 33 | 45 \pm 10 | 130 \pm 30 | 0.67 \pm 0.27 | 7.47 $^{+1.50}_{-1.50}$ | AGN / AGN |
| | | | 6.9 \pm 0.9 | 1623 \pm 213 | 73 \pm 10 | | | | Broad line cmpt |
| SMM J123707.21+621408.1 | 3.6 | 2.490[5] | 1.6 \pm 0.5 | 348 \pm 40 | 35 \pm 8 | 88 \pm 24 | ... | 5.48 $^{+2.03}_{-1.58}$ | SB / SB |
| SMM J123711.32+621331.3 | 2.4 | 1.9958[4] | 0.4 \pm 0.3 | 112 \pm 18 | 10 \pm 5 | 16 \pm 9 | < 0.05 | 5.48 $^{+2.03}_{-1.58}$ | int / SB |
| SMM J123711.98+621325.7 | 2.4 | ... | < 0.25 | ... | < 5 | < 6 | ... | 3.88 $^{+1.05}_{-0.82}$ | SB / ... |
| SMM J131205.60+423946.0 | 2.4 | ... | < 0.3 | ... | < 6 | < 8 | ... | 5.50 $^{+2.00}_{-2.00}$ | SB / ... |
| RGJ 131208.34+424144.4 | 2.4 | 2.2372[18] | 0.9 \pm 0.2 | 448 \pm 60 | 24 \pm 5 | 32 \pm 18 | 1.20 \pm 0.60 | 5.13 $^{+2.00}_{-1.05}$ | SB / AGN |
| | | | 0.9 \pm 0.8 | 959 \pm 100 | 26 \pm 5 | | | | Broad line cmpt |
| SMM J131208.82+424129.1 | 2.4 | 1.5439[6] | 6.1 \pm 2.3 | 387 \pm 60 | 103 \pm 15 | 111 \pm 32 | 0.20 \pm 0.15 | 3.23 $^{+0.15}_{-0.19}$ | SB / AGN |
| | | | 2.1 \pm 1.0 | 450 \pm 80 | 120 \pm 20 | | | | Broad line cmpt |
| RGJ 131236.05+424044.1 | 2.4 | 2.2402[8] | 2.3 \pm 1.2 | 447 \pm 75 | 20 \pm 6 | 106 \pm 40 | 0.22 \pm 0.08 | 6.69 $^{+0.59}_{-0.59}$ | SB / SB |
| SMM J163639.01+405635.9 | 2.4 | 1.4880[6] | 8.9 \pm 3.0 | 248 \pm 25 | 188 \pm 35 | 147 \pm 48 | 0.30 \pm 0.20 | 5.47 $^{+1.88}_{-1.50}$ | SB / SB |
| SMM J163650.43+405734.5 | 4.8 | 2.3850[5] | 12.2 \pm 2.0 | 306 \pm 47 | 105 \pm 20 | 58 \pm 19 | 0.41 \pm 0.10 | 50.5 $^{+15.0}_{-15.8}$ | int / AGN |
| | | | 12.0 \pm 1.0 | 1753 \pm 238 | 1236 \pm 200 | | | | Broad line cmpt |
| SMM J163655.80+405914.0 | 2.4 | 2.5918[6] | 2.4 \pm 0.4 | 225 \pm 29 | 336 \pm 60 | 102 \pm 15 | 0.45 \pm 0.10 | 10.89 $^{+2.21}_{-3.75}$ | AGN / AGN |
| | | | 16 \pm 2 | 2962 \pm 402 | 254 \pm 40 | | | | Broad line cmpt |
| SMM J163658.19+410523.8 | 2.4 | 2.4482[6] | 1.9 \pm 0.4 | 364 \pm 77 | 76 \pm 15 | 71 \pm 35 | 0.65 \pm 0.3 | 10.90 $^{+2.25}_{-3.77}$ | SB / SB |
| SMM J163706.51+405313.8 | 2.4 | 2.3745[9] | 4.7 \pm 0.6 | 225 \pm 29 | 96 \pm 15 | 160 \pm 20 | 0.27 \pm 0.04 | 7.17 $^{+4.21}_{-3.00}$ | AGN / AGN |
| | | | 2.7 \pm 0.8 | 3317 \pm 987 | 125 \pm 15 | | | | Broad line cmpt |
| ISAAC VLT | | | | | | | | | |
| SMM J221733.91+001352.1 | 3.0 | 2.5510[7] | 8.5 \pm 3.5 | 198 \pm 98 | 30 \pm 10 | 254 \pm 128 | ... | 4.94 $^{+1.88}_{-2.63}$ | SB / SB |
| Narrow-band imaging | | | | | | | | | |
| NSFCAM IRTF | | | | | | | | | |
| SMM J105230.73+572209.5 | 12.6 | 2.610[5] | 1.2 \pm 0.5 | ... | ... | 21 \pm 8 | ... | 10.3 $^{+0.75}_{-1.13}$ | SB / ... |
| SMM J123635.59+621424.1 | 9.0 | 2.005[5] | 8.1 \pm 1.0 | ... | ... | 181 \pm 20 | ... | 7.47 $^{+1.50}_{-1.50}$ | AGN / ... |
| SMM J131215.27+423900.9 | 7.2 | 2.565[5] | 11.8 \pm 1.0 | ... | ... | 493 \pm 41 | ... | 13.90 $^{+0.33}_{-2.48}$ | AGN / ... |
| SMM J140104.96+025223.5 | 9.0 | 2.565[5] | 1.2 \pm 0.2 | ... | ... | 47 \pm 10 | ... | 6.76 $^{+2.50}_{-2.50}$ | AGN / ... |
| SMM J163631.47+405546.9 | 14.4 | 2.283[5] | 0.30 \pm 0.19 | ... | ... | 10 \pm 6 | ... | 10.97 $^{+6.76}_{-4.73}$ | AGN / ... |
| UFTI UKIRT | | | | | | | | | |
| SMM J105226.61+572113.0 | 22.7 | 2.425[5] | 0.78 \pm 0.1 | ... | ... | 27 \pm 4 | ... | 2.40 $^{+1.40}_{-1.40}$ | SB / ... |
| SMM J131232.31+423949.5 | 15.0 | 2.300[5] | 1.9 \pm 0.1 | ... | ... | 58 \pm 5 | ... | 14.80 $^{+0.98}_{-2.93}$ | SB / ... |

Note the value given in the [] z column is the error in the last decimal place. The H α flux given in column 4 is the narrow line H α flux unless otherwise stated. The H α fluxes are the observed flux (not corrected for slit flux losses or atmospheric transmission), but the SFR's have had both corrections applied (where applicable). The H α star-formation rates are uncorrected for extinction. H α classifications are described in §2.4 (SB=star burst; int=intermediate, AGN=AGN).

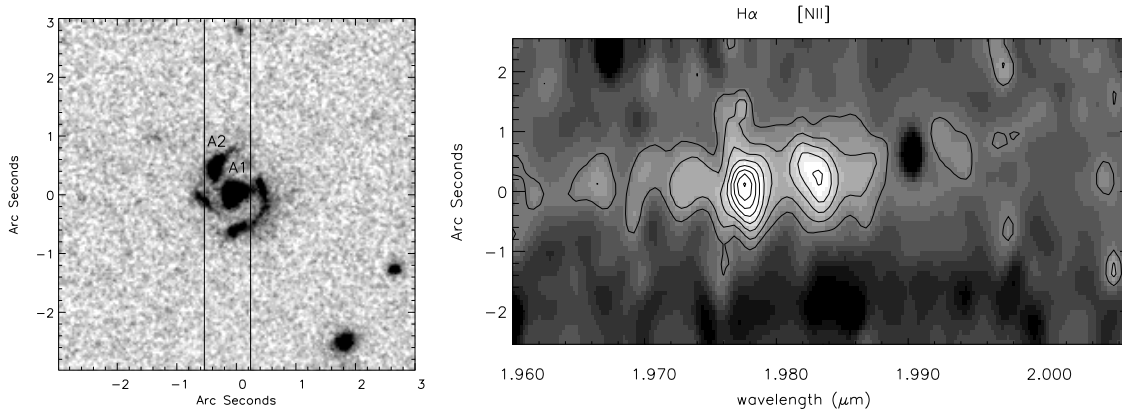


FIG. 2.— *Left*: Combined B , V and I -band *HST* ACS observations of SMMJ123635.59+621424.1 with the slit position overlaid. *Right*: The position-velocity diagram around the $H\alpha$ line from the NIRSPEC near-infrared spectrum of the galaxy. This shows an apparent $\sim 100 \text{ km s}^{-1}$ velocity gradient in the $H\alpha$ emission line and a somewhat larger velocity gradient, $\sim 150 \text{ km s}^{-1}$, in $[\text{NII}]$. The central component of the galaxy (labeled A1) has an $[\text{NII}]/H\alpha$ ratio of 0.60 ± 0.15 and hosts a bright, unresolved radio source (Chapman et al. 2004a); both features suggest that it contains an AGN. A1 is offset from A2 by $\sim 150 \text{ km s}^{-1}$ in velocity and around 3 kpc in projection on the sky. A2 has an $[\text{NII}]/H\alpha$ ratio of 0.2 ± 0.1 , suggesting that this is a star-forming knot or close companion. Here $1''$ corresponds to 8.4 kpc at the redshift of this galaxy and the image has been rotated to match the position angle of the spectrum.

We also have a second SFR indicator for our sample of SMGs/OFRGs – their far-infrared (FIR) luminosities. A significant fraction of the bolometric luminosity of the most active dusty galaxies is absorbed by interstellar dust and re-emitted in the thermal IR, at wavelengths $10\text{--}300 \mu\text{m}$. If young stars dominate the radiation output in the UV-visible wave band and the dust opacity is high everywhere, then the far-infrared luminosity measures the bolometric luminosity of the star-burst and this in turn provides an excellent tracer of the SFR of the galaxy. Adopting the models of Leitherer et al. (1995) for continuous bursts of age $10\text{--}100 \text{ Myr}$ and using the same IMF as in the $H\alpha$ calculation yields $\text{SFR}(M_{\odot} \text{ yr}^{-1}) = 4.5 \times 10^{-37} L(\text{FIR}) W$ (Kennicutt et al. 1998). We stress that this relation only holds if the age of the star-burst is less than 100 Myr .

We list the SFR and $H\alpha$ flux measurements from our sample in Table 2. We also give the far-infrared luminosities of these galaxies from Chapman et al. (2003a, 2004b). These values are derived from fitting model spectral energy distributions (SEDs) to the observed $850 \mu\text{m}$ and 1.4-GHz fluxes of the galaxies at their known redshifts, assuming that the local far-infrared–radio correlation holds (Condon et al. 1991; Garrett 2002).

2.6. Notes on Individual Galaxies

Observations of six of the galaxies in our sample are particularly noteworthy and so we discuss these in more detail here.

SMMJ123635.59+621424.1 — Dawson et al. (2003) identified this object as a $z=2.015$ spiral galaxy, but their near-infrared spectroscopy around the $H\alpha$ emission line shows a $2500 \pm 250 \text{ km s}^{-1}$ broad-line $H\alpha$ component and $[\text{NII}]/H\alpha$ emission line flux ratio 0.45 ± 0.1 . The presence of the broad-line component and detection of hard ($\Gamma = 0.3$) X-ray emission from *Chandra* imaging indicate an obscured type II AGN (Dawson et al. 2003). Our spectroscopic and narrow-band observations of this galaxy produce comparable $H\alpha$ fluxes, which, along with the compact morphology of the galaxy in the IRTF narrow-band image, suggests that the spectroscopic slit is sampling the bulk of the emission from this system (the slightly lower flux in the narrow-band observation arises because the

narrow-filter only samples the narrow-line $H\alpha$; $\sim 20\%$ of the broad-line flux is missed). Our spectroscopic observations of this target show clear velocity structure in the $H\alpha$ and $[\text{NII}]$ emission lines (Fig. 2). We aligned the slit with the center of the galaxy and the bright knot (labeled A2 in Fig. 2), and our resulting Keck spectroscopic observations indicate either a velocity shear or rotation in the $H\alpha$ emission line with an amplitude of $\sim 100 \text{ km s}^{-1}$ within $\sim 2''$ (17 kpc in projection) along the slit (Fig. 2). By collapsing down the $H\alpha$ and $[\text{NII}]$ emission lines in the spectral direction, we find an offset of $0.3''$ (3 kpc) along the slit between the maximum intensities of these two lines, as well as an associated variation in the $[\text{NII}]/H\alpha$ ratio from $\sim 0.2 \pm 0.1$ up to $\sim 0.60 \pm 0.15$ (which is consistent with the results of Dawson et al. 2003). We also find a similar broad-line component to the $H\alpha$ emission, confirming the presence of an AGN. The high-resolution *Hubble Space Telescope*⁹ (*HST*) ACS image of this galaxy (Fig. 2), from the GOODS imaging of this region (Giavalisco et al. 2004; Dawson et al. 2003; Smail et al. 2004), shows an apparently face-on spiral galaxy with a bright nucleus (A1) and a prominent companion or knot in one of the spiral arms (A2); the optical extent of the galaxy is 13 kpc ($1.5''$). The separation between the nucleus (A1) and knot (A2) in the image is $\sim 0.5''$ (5 kpc) – comparable to the apparent offset in the emission-line peaks. The high-resolution 1.4-GHz MERLIN map of this galaxy in Chapman et al. (2004c) shows an unresolved radio source coincident with the nuclear component, which is also where the $[\text{NII}]/H\alpha$ is the strongest (~ 0.6), providing further support for the classification of this component as an AGN. The face-on aspect of this system, combined with the modest velocity difference between A1 and A2, suggests to us that the latter may be a dynamically-distinct component (rather than a star-forming knot inside a spiral arm), an interaction which has prompted the activity we see. We note that it is possible for intensity gradients between separate components to mimic velocity gradients as a result of the way in which long-slit spectroscopy mixes spatial and spectral domains. However, the spatial offset between A1 and A2 in the dispersion direction is $\sim 0.4''$, corresponding to $10A$, which is much less than the apparent velocity gradient. We therefore

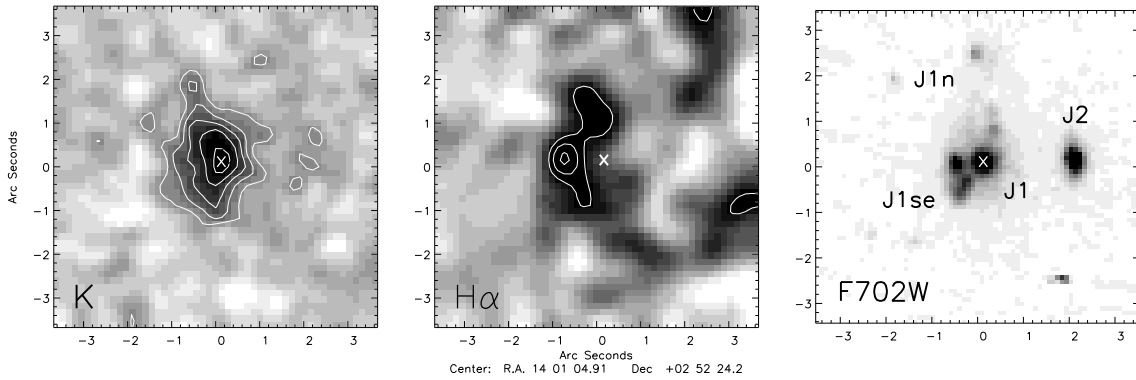


FIG. 3.— Three views of SMM J140104.9: broadband K image from IRTF (*left*); $H\alpha$ continuum-subtracted, narrow-band image from IRTF (*middle*) and the HST R_{702} -band of the system which illustrates its very complex morphology (*right*). We identify in the HST image the three main components of this galaxy as defined by Ivison et al. (2001), and in each panel we also mark the position of the peak of component J1. It is clear that the optical-near-infrared colors and $H\alpha$ surface brightness of component J2 are much different from those of J1n and J1se – ruling out the suggestion that J2 represents a lensed counter-image of J1n or J1se (Downes & Solomon 2003). Moreover, the $H\alpha$ emission extending south from J1n and wrapping around J1 traces the morphology of the clumps visible in the R -band, J1se, and has no significant contribution from the smooth component, J1. We discuss the interpretation of this result in more detail in §3.1

suggest that the velocity offset most likely arises from motions within the galaxy, rather than as an artifact of the observation.

SMM J123707.21+621408.1 — We observed this target with a position angle such that the NIRSPEX slit passes through the two components shown in the HST ACS imaging in Smail et al. (2004). This galaxy consists of a red component and a much bluer object separated by $0.2''$ (1.7 kpc; labeled B1 and B2 in Fig 5). The resulting NIRSPEX spectrum shows two strong, spatially-extended lines separated by ~ 600 km s^{-1} . We identify both of these emission lines as $H\alpha$ (rather than $H\alpha$ and $[\text{NII}]$) from two separate components for two reasons: (1) the spatial separation between the two components in the spectra is matched almost exactly by the separation in the HST ACS image (Fig. 5); and (2) if the higher velocity component was identified as strong $[\text{NII}]\lambda 6583$ then the line ratio would be $[\text{NII}]/H\alpha \sim 1$, and yet we see no signs of the $[\text{SII}]$ emission line, which has a ratio of $[\text{SII}]/[\text{NII}] \sim 0.5$ for AGN (Ferland & Osterbrock 1986).

SMM J123711.32+621331.3 — This target was known to consist of two radio sources, both of which may contribute to the far-infrared emission. Aligning the slit along both components, we detect only faint continuum and no lines from the UV-identified component, SMM J123711.98+621325.7, for which Chapman et al. (2004a) measured the redshift of the system. However, we do detect $H\alpha$ emission from the second radio source, SMM J123711.32+621331.3. This allowed us to derive a redshift of 1.9958 ± 0.0004 , giving an offset of 400 ± 50 km s^{-1} and $8''$ (~ 70 kpc) in projection from SMM J123711.98+621325.7.

RGJ 131236.05+424044.1 — The ground-based K -band imaging of this galaxy from Smail et al. (2004) shows a bright nucleus surrounded by a diffuse halo approximately $2''$ (16 kpc) in extent. The two components seen in the near-infrared spectrum are separated by $\sim 185 \pm 45$ km s^{-1} in velocity and $0.4''$ (3.4 kpc) in projection. The two-dimensional near-infrared spectrum suggests that one of the sources (labeled C1) displays signs of a velocity shear in $H\alpha$ across $\sim 0.5''$. The $[\text{NII}]/H\alpha$

ratio shows marginal evidence for variation from 0.45 ± 0.10 to 0.35 ± 0.10 between C1 and C2 and also mimics the velocity offset between C1 and C2. These modest $[\text{NII}]/H\alpha$ emission line ratios indicate that both components are likely to be starburst, rather than AGN-, dominated.

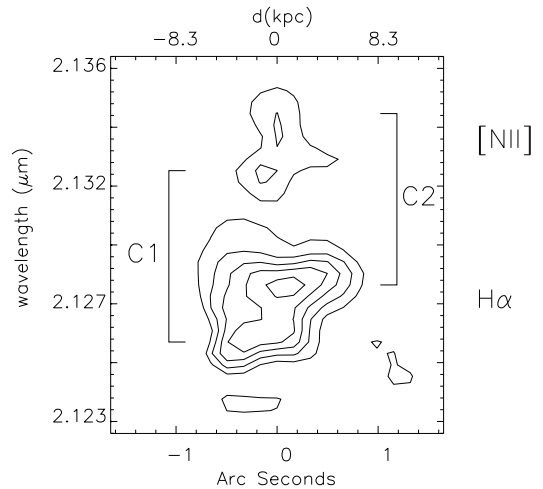


FIG. 4. – Two Dimensional near-infrared spectrum of RGJ 131236.05, showing the velocity structure seen in $H\alpha$ and $[\text{NII}]$. We identify two components (labeled C1 and C2), offset by 185 ± 40 km s^{-1} and 3.4 kpc in projection along the slit.

SMM J140104.96+025223.5 — This $z = 2.56$ sub-mm selected galaxy (SMM J14011+0252) is discussed in detail by Ivison et al. (2000, 2001). It lies in the field of the $z = 0.25$ cluster A 1835 and is expected to be amplified by a factor of 2.75 by the foreground cluster potential. The morphology of this galaxy is complex (Fig. 3). Ivison et al. (2001) identify three main components: J1, a blue relatively smooth and regular object; J2, a bluer and more compact object about $2''$ to the west of J1; and J1n, an extremely red, diffuse structure which extends 2 – $3''$ to the north of J1.

The interpretation of this multi-component system is con-

⁹Based on observations made with the NASA/ESA *Hubble Space Telescope* which is operated by STSCI for the Associate of Universities for Research in Astronomy, Inc., under NASA contract NAS5-26555

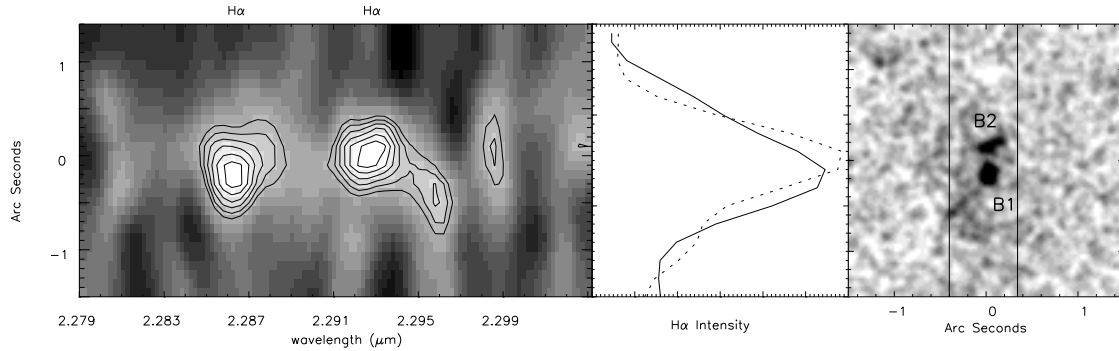


FIG. 5.— *Left*: Position-velocity diagram around the $H\alpha$ line from the near-infrared spectrum of SMM J123707.21. *Right*: Combined B -, V - and I -band *HST* ACS observations of this galaxy with the slit position overlaid. *Middle*: Intensity distribution of the $H\alpha$ emission collapsed over the central 200 km s^{-1} of each of the two $H\alpha$ emission lines. This shows an apparent spatial offset of $0.2''$ (and 600 km s^{-1} velocity offset) between the two galaxies. This matches the apparent separation of the central component of the galaxy (labeled B1) from the much redder second component (labeled B2) which are offset by 2 kpc in projection. (For a color version of this image, see Smail et al. 2004).

tentious. Ivison et al. (2001) suggest that the gas reservoir and source of the far-infrared emission from this galaxy reside in J1n – with J2 and J1 simply being less-obscured components within the same system. However, Downes & Solomon (2003) suggest that the clumpy features to the south-west of J1 (called J1se), as well as J1n and J2, are all images of a single, highly-amplified background sub-mm source – which is being lensed by both the regular component of J1 (which they identify as a foreground ($z \sim 0.20$) galaxy) and the cluster potential.

Our IRTF continuum-subtracted $H\alpha$ image provides a powerful tool for testing these competing suggestions (see also Tecza et al. 2004). We compare the morphology of the $H\alpha$ emission with the R_{702} - and K -band images in Fig. 3. It is clear that the bulk of the emission traces components J1 and J1se, with the regular J1 and compact J2 being undetected. This immediately rules out the possibility that J2 is a lensed counter-image of J1n or J1se. However, the absence of $H\alpha$ emission from the smooth component of J1 is a concern – suggesting that the claim by Downes & Solomon (2003) that it is a foreground lens may be correct. To further test this, we have returned to the optical spectrum of J1 presented by Barger et al. (1999) and claimed by them to represent a classical Lyman-break galaxy. More careful study of this spectrum leads us to re-examine this interpretation: there are strong absorption features at 4745, 4784, 4912, 4957, 5374, and 6070Å, which are unidentifiable at the redshift claimed by Barger et al., $z = 2.55$, but correspond exactly to Balmer $H\zeta$, $H\eta$, Ca H&K, G-band and $H\beta$ absorption at $z = 0.248$. This is an unfortunate conjunction – J1 is a $\sim 0.1L^*$, post-starburst member of the A 1835 cluster. The absence of any strong emission lines in this galaxy and broadband colours which are much bluer than the typical passive E/S0 cluster member mean that its nature is not immediately obvious from either the published spectrum or the true colour images of the cluster (Ivison et al. 2000, 2001).

How does this effect the interpretations of SMM J140104.96 by Downes & Solomon (2003) and Ivison et al. (2001)? We confirm that J1 is a foreground lens as stated by Downes & Solomon (2003). However, our observations disprove their central claim that J1n, J1se, and J2 are highly-amplified multiple images of an intrinsically low-luminosity sub-mm source. In fact, J1n/J1se and J2 are probably single images of three background galaxies at $z = 2.56$ (see Tecza et al. 2004), with the $H\alpha$ emission from this system arising entirely from very red

J1n/J1se – which is also the site of a massive gas reservoir and hence most likely the far-infrared source (Frayser et al. 2003; Ivison et al. 2001). The addition of J1 to the foreground lens model does increase the estimate of the area-averaged amplification for J1n/J1se from 2.5 to ~ 5 ; however, this does not significantly alter any of the conclusions in Ivison et al. (2001).

SMM J163650.43+405734.5 — We also observed SMM J163650.43 (ELAIS-N2 850.4, Smail et al. 2003) using NIRSPEC for a total of 4.8 ks at two orthogonal position angles. The detailed kinematics of this complex merging system using three dimensional near-infrared spectroscopy will be discussed in Swinbank et al. 2005. However, we note that the broad $H\alpha$ component is apparently offset from the narrow $H\alpha$ component by $\sim 300 \text{ km s}^{-1}$. The redshift quoted in Table 2 is that of the narrow line $H\alpha$.

2.7. $H\alpha$ Properties of SMGs

We show near-infrared spectra of the 23 detected galaxies from our Keck and VLT observations in Fig. 1 marked with the expected redshifts of lines based on the best-fit $H\alpha$ redshift (Table 2). As these were short exposures, primarily meant to derive redshifts, the signal-to-noise ratio on the individual galaxies is generally modest. To overcome this, we have also combined all of the spectra to provide a composite near-infrared spectrum for a representative far-infrared luminous galaxy at $z \sim 2.4$.

We create the composite spectrum by de-redshifting and summing all of the spectra (normalised by $H\alpha$ flux) for our galaxies (we note that stacking the spectra based on their individual signal-to-noise ratio or an unweighted stack does not alter any of the conclusions below). We also derive a composite spectrum for those galaxies which individually show no signs of an AGN (i.e., those with small $[\text{NII}]/H\alpha$ ratios and line widths). The resulting composite spectra are shown in Fig. 6. The rest-frame composite spectrum from the entire sample is best fit ($> 99\%$ confidence level) with an underlying broad-line region with a narrow-to-broad line flux ratio of 0.6 ± 0.1 and $\text{FWHM}_{\text{rest}}$ of $1300 \pm 210 \text{ km s}^{-1}$ for the broad-line $H\alpha$ and $325 \pm 30 \text{ km s}^{-1}$ for the narrow-line $H\alpha$. The average $[\text{NII}]/H\alpha$ for the entire sample is 0.42 ± 0.05 which is indicative of star formation.

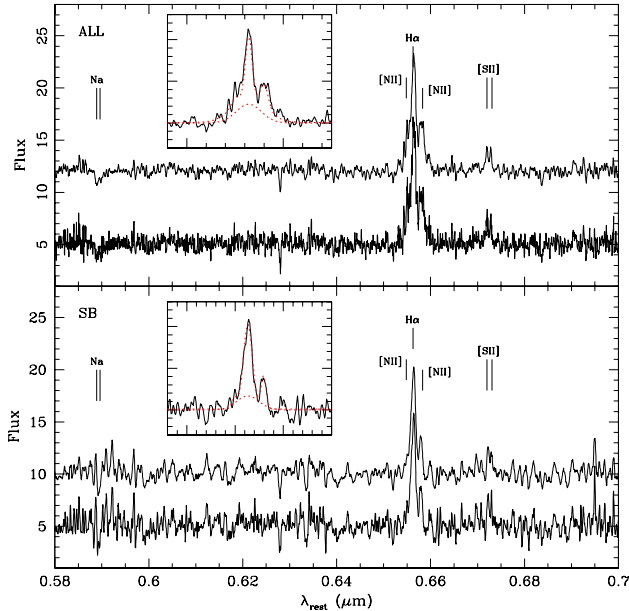


FIG. 6. – Rest-frame composite spectrum of all of the galaxies in our sample (*top*) and well as the composite from the (individually spectroscopically classified) star-forming galaxies (*bottom*) (we have not included SMMJ123707.21 in either composite as we believe that the spectra display two $H\alpha$ components coming from two interacting galaxies rather than $H\alpha$ and $[NII]$). The insets show the region around the $H\alpha$ emission line with the best fit to the emission line using four Gaussian profiles overlaid. We also show the broad line component of the best-fit. The average $[NII]/H\alpha$ ratio is 0.42 ± 0.05 for the entire sample and 0.19 ± 0.05 for the star-forming galaxies. Both are consistent with star-forming galaxies rather than an AGN. We also detect the $[SII]\lambda\lambda 6716, 6731$ emission doublet (marginally detected in the SB sample) and the (unresolved) stellar $Na\lambda\lambda 5889.95, 5895.92$ absorption doublet. By fitting the Na absorption and $[SII]$ doublets, we find no velocity offset from $H\alpha$. The $[SII]/H\alpha$ ratio can be used to classify the SMGs/ORFGs optical emission line properties as LINER- or HII-region-like. While the SMGs/ORFGs which are individually classified as star-forming galaxies show no signs of an underlying broad $H\alpha$ line, the composite from this subsample of galaxies is best fit with a narrow/broad $H\alpha$ emission line ratio of 0.45 ± 0.20 .

The $[SII]/H\alpha$ ratio can be used to classify the spectral type of galaxies (Veilleux et al. 1995). The wavelengths of the $[SII]\lambda\lambda 6716, 6731$ lines in the composite spectra are 6722 ± 6 and $6729 \pm 5\text{\AA}$ – indicating no detectable velocity offset between the $H\alpha$ and $[SII]$ emission lines. From the strengths of the lines we estimate a ratio of $[SII]/H\alpha = 0.10 \pm 0.04$ – placing the composite SMG/ORFG within either the LINER or HII region of the classification space (Veilleux et al. 1987, 1995). This is similar to the typical optical spectral classification of local ULIRGs, for which mid-infrared observations (Lutz et al. 1999) and spatially-resolved spectroscopy (Heckman et al. 1990) both suggest that star-formation is the dominant power source (see Lutz et al. 1999).

The composite spectrum also shows an absorption feature at a wavelength close to that expected for the Na doublet which is seen from cool stars and from the warm neutral ($T \sim 10^4$ K) phase of the interstellar medium (ISM; Phillips 1993). This has been used to map the velocity structure of large-scale outflows from nearby ULIRGs (Heckman et al. 2000; Rupke et al. 2002). For a galaxy whose light is dominated by a young star-burst, as we believe is the case for these SMGs/ORFGs,

the warm ISM is expected to be the primary source of this absorption feature. We fit the Na absorption line with two Gaussian profiles with a fixed separation and variable width and derive a central wavelength of $5889 \pm 5\text{\AA}$, which is entirely consistent with the rest-frame wavelength of the resolved doublet ($\lambda\lambda 5889.95, 5895.92\text{\AA}$). We thus place a limit of $< 150 \text{ km s}^{-1}$ on the possible velocity offset of this feature from the $H\alpha$ redshift. The $FWHM_{\text{rest}}$ of the Na lines is $292 \pm 192 \text{ km s}^{-1}$, which is also consistent with the FWHM of the $H\alpha$ emission in the rest-frame composite.

The composite spectrum thus shows no signs of an offset in velocity between Na or $[SII]$ and $H\alpha$. This is slightly surprising since many local luminous/ultra-luminous infra-red galaxies display velocity offsets of several 100 's km s^{-1} between these lines (Heckman et al. 2000; Rupke et al. 2002). We defer a detailed discussion of the velocity offsets between the UV ISM and (star-burst) nebular emission lines in the individual galaxies to a later paper (Smail et al. in prep).

Turning to the rest-frame composite from those galaxies which individually show no signs of an AGN component (i.e. those with low $[NII]/H\alpha$ emission line ratios and small $H\alpha$ line widths), we fit this spectrum with both $[NII]\lambda\lambda 6548, 6583$ emission lines and also attempt to fit a broad line $H\alpha$ component. When the broad component is included in the fit, the total χ^2 is marginally better than when the broad component is excluded, with a change in the total $\chi^2 = 4$ which corresponds to $\sim 2\sigma$ (or $\sim 87\%$ confidence). The resulting best-fit model for the SB composite has an underlying broad-line $H\alpha$ component with a ratio of broad-line/narrow-line $H\alpha = 0.45 \pm 0.20$ and a broad-line $FWHM_{\text{rest}} = 890 \pm 210 \text{ km s}^{-1}$, suggesting that even the SMGs/ORFGs which are identified individually as star-bursts may contain at least some level of underlying non-thermal activity. Nevertheless, the $[NII]/H\alpha$ emission line ratio is 0.19 ± 0.05 , which, along with the limit of $[SII]/H\alpha \lesssim 0.14$, still suggests that the energy output is star-formation-, rather than AGN- dominated.

2.8. Kinematics of $H\alpha$ emission

The narrow $H\alpha$ emission line of the SB composite has a rest-frame $FWHM_{\text{rest}}$, after correcting for the instrumental resolution of the observations, of $FWHM_{\text{rest}} = 400 \pm 70 \text{ km s}^{-1}$ – in agreement with the average $H\alpha$ line width from the SMGs/ORFGs which make up this composite spectrum ($350 \pm 50 \text{ km s}^{-1}$). This is somewhat larger than the $H\alpha$ line widths of UV-selected galaxies at $z \sim 2$ identified by Erb et al. (2003), who derive a mean $FWHM_{\text{rest}} = 242 \pm 65 \text{ km s}^{-1}$ for their sample. We compare the distribution of line widths for these two populations (as a function of their $H\alpha$ luminosities) in Fig. 7. We see that the SMGs/ORFGs are typically 6 times brighter in $H\alpha$ (*before* any correction for reddening) than the UV-selected population at their epoch. More interestingly, the emission line widths of the SMGs/ORFGs are on average $\sim 50\%$ larger than those measured for the UV-selected systems, although the two distributions overlap substantially. This difference could reflect either: (1) different halo masses, (2) different dynamical states, (3) a contribution from a broad AGN component in some SMGs/ORFGs, or (4) starburst-driven superwinds contributing to the line widths. The composite spectra from §3.2 certainly suggest that an unidentified broad component to the $H\alpha$ emission may be present in some SMGs/ORFGs – however, as we show below, we do not believe that this is the chief cause of the difference in the line widths of the two populations.

We first compare our $H\alpha$ -derived line widths with those ob-

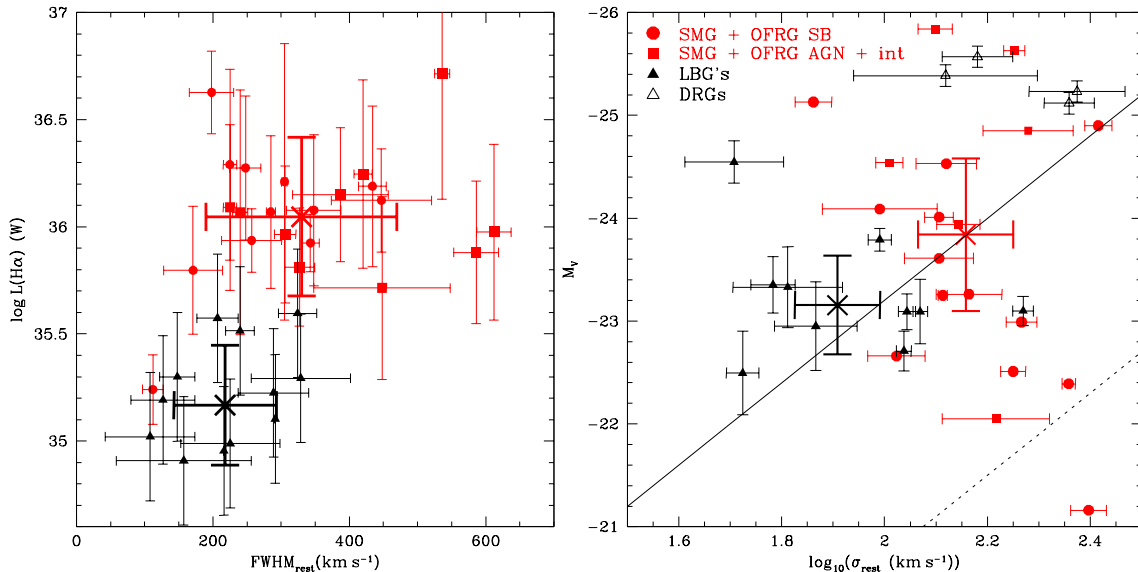


FIG. 7.— *Left*: Comparison of the $H\alpha$ luminosity vs $\text{FWHM}_{\text{rest}}$ for the narrow $H\alpha$ components (deconvolved for instrumental resolution) in our sample compared to those found in UV-selected galaxies by Erb et al. (2003; we have conservatively assumed a factor of two uncertainty in the $H\alpha$ luminosities for this sample). We also include those galaxies which show single broad lines (no narrow component). The crosses mark the positions of the median luminosity and $\text{FWHM}_{\text{rest}}$ for the two populations. The line widths in the SMGs/OFRGs have a median of 330 km s^{-1} and a long tail out to $\sim 600 \text{ km s}^{-1}$. In comparison to the UV-selected galaxies studied by Erb et al. (2003) (which have a median of $\sim 210 \text{ km s}^{-1}$), SMGs/OFRGs appear to be typically more massive systems, with a wider distribution of line widths (although some of the broadest lines may come from unresolved companions or AGN). *Right*: Correlation between rest-frame optical emission line width and rest-frame V -band luminosity (the Faber–Jackson relation) for the SMGs/OFRGs compared to the LBGs and DRGs from Pettini et al. (2001) and van Dokkum et al. (2004). The crosses mark the positions of the median luminosity and σ_{rest} for the SMGs/OFRGs and LBGs. We show the local Faber–Jackson relation by the dotted line (assuming $V-R=0.3$) and also the same line offset by a further 2.5 magnitudes in order to pass through the median of the SMG sample (solid line).

tained from the dynamics of cold gas as traced by interferometric maps of the CO distributions in a small number of SMGs (Frayer et al. 1999; Neri et al. 2003; Genzel et al. 2003). The sample of five galaxies compiled by Neri et al. (2003) have a $\text{FWHM}_{\text{rest}}$ for the CO of $420 \pm 35 \text{ km s}^{-1}$ and a mean ratio of $H\alpha$ to CO FWHM consistent with unity (1.27 ± 0.24) for the four galaxies in common with our sample. The CO line widths are unaffected by the presence of any AGN or large-scale winds, and so this suggests that the AGN or superwind contribution to the $H\alpha$ line widths for SMGs/OFRGs may not be responsible for the comparatively large $H\alpha$ line widths.

We can therefore combine the emission-line widths for our sample with the typical physical extent of the $H\alpha$ emission from our narrow-band imaging of the SMGs/OFRGs to place limits on their masses. The spatial extent of the $H\alpha$ in the galaxies has a wide distribution: $\lesssim 0.5\text{--}1.0''$ (corrected for seeing) or $\lesssim 4\text{--}8 \text{ kpc}$ (c.f. Smail et al. 2004). Assuming that the $H\alpha$ emission arises from virialised clouds in the galaxy’s potential well, we estimate a typical mass of $1\text{--}2 \times 10^{11} M_{\odot}$ for the SMGs/OFRGs in our sample (Erb et al. 2003), with corresponding dynamical times of $10\text{--}20 \text{ Myr}$. Using the limits on the spatial extent of the CO emission, Neri et al. (2003) determine a median dynamical mass of $\sim 6 \times 10^{10} M_{\odot}$ assuming that the CO gas is in bound orbits. Thus, the masses derived from the dynamics of the cold gas in a small sample of these galaxies support those estimated from the emission-line kinematics.

The masses of UV-selected galaxies at $z \sim 2$ derived in an identical manner by Erb et al. (2003) have a median of $3.3 \pm 1.1 \times 10^{10} M_{\odot}$, around 5 times lower than our estimates for the SMGs/OFRGs. This is due to a combination of smaller estimated sizes and lower $H\alpha$ line widths. Clearly both of these estimates have large systematic errors, yet they are suggestive of a real difference in the characteristic masses (or dynamical

states) of restframe UV- and far-infrared selected galaxies at $z \gtrsim 2$.

We can also obtain an independent measure of the masses of the SMGs/OFRGs from the seven galaxies which show multiple components and for which we have estimates of the velocity differences between the components. Assuming random orientations on the sky and that the components are bound/merging, the masses of the systems are $\sim 1.5 \pm 0.9 \times 10^{11} M_{\odot}$. This is comparable to the earlier estimates and gives us confidence that the SMGs/OFRGs are indeed massive galaxies.

2.9. Magnitude – Line Width correlations

Correlations between rest-frame luminosity and kinematics (as measured by the widths of the emission lines) at high redshift have had only limited success. Pettini et al. (2001) and van Dokkum et al. (2004) have attempted to study the Tully–Fisher-like or Faber–Jackson-like (Tully & Fisher 1977; Faber & Jackson 1976) correlations for LBGs and distant red galaxies (DRGs) at $z \gtrsim 2$; however, no correlations have been found over the range $\text{FWHM}_{\text{rest}} \sim 120\text{--}300 \text{ km s}^{-1}$. This may be due in part to the small sample sizes involved. To search for such a correlation, the SMGs for which we have well-defined narrow-line $H\alpha$ line width measurements can be added to this sample. We compute the de-reddened rest-frame V -band magnitudes for the SMGs in our sample by using HYPER-Z (Bolzonella et al. 2000) to compute the best-fit SED to the observed IJK photometry from Smail et al. (2004). We also convert $\text{FWHM}_{\text{rest}}$ to σ by assuming $\text{FWHM} = 2.35 \times \sigma$.

Fig. 7 shows the resulting luminosity–line width correlation for the combined sample of SMGs, LBGs, and DRGs (the latter two from Pettini et al. (2001) and van Dokkum et al. (2004) are corrected for reddening using their estimates of A_V). We also overlay the local Faber–Jackson relation from Jørgensen et al.

(1995, 1999; assuming $V - R = 0.3$), and fit the zero-point of the same correlation so that it passes through the median of the SMG sample – resulting in an offset of 2.5 mag. This offset is comparable to the $\Delta_{\text{fade}} V$ found in Smail et al. (2004) and suggests that the descendants of these high redshift populations are likely to lie on or around the local Faber–Jackson relation.

2.10. SFR Comparisons

Next we compare the far-infrared and $H\alpha$ luminosities of the galaxies in our sample to investigate the influence of AGN and star formation power-sources and the possible effects of dust extinction on the $H\alpha$ emission from this population.

Fig. 8 compares the $H\alpha$ and far-infrared luminosities of the galaxies in our sample. We have also included measurements from the literature from five well-studied dusty, high-redshift galaxies: SMM J02399–0136 (Ivison et al. 1998, 2000), SMM J17142+5016 (Smail et al. 2003), ERO J164502+4626 (Dey et al. 1999), SMM J04431+0210 (Frayser et al. 2003), and SMM J16359+6612 (Kneib et al. 2004).

The star formation rate derived from the far-infrared and $H\alpha$ should be correlated if the effects of dust and any contributions from AGN are uniform across the sample. The SMGs/OFRGs in our sample show only a weak correlation between SFR(FIR) and SFR($H\alpha$), with comparable scatter in the $H\alpha$ -derived SFR and that estimated from the far-infrared ($\Delta(\text{FIR})/\text{FIR} = 0.30 \pm 0.18$ vs. $\Delta(H\alpha)/H\alpha = 0.37 \pm 0.20$). Reassuringly, the two galaxies for which we failed to obtain $H\alpha$ detections in good conditions are also two of the least luminous galaxies when ranked on their far-infrared emission.

We have also included in Fig. 8 samples of similar and less luminous far-infrared galaxies from surveys of the $z < 1$ universe. These come from ISOCAM-selected galaxy surveys (Franceschini et al. 2003; Flores et al. 2004) and studies of local Very- and Ultra-Luminous infrared galaxies by Poggianti & Wu (2000) and Dopita et al. (2002). Compared to these samples, we see a similar wide dispersion in the ratio of far-infrared to $H\alpha$ luminosities across a factor of nearly 100 in far-infrared luminosity. This is suggestive of a similar diversity in the energy sources and obscuration for galaxies with far-infrared luminosities from $10^{10} - \gtrsim 10^{12} L_{\odot}$. In support of this, we note that the distribution of $H\alpha$ equivalent widths (EW, Table 2) for the SMG sample peaks at about ~ 20 –40Å and has a long tail out to $\gtrsim 100$ Å, with a median $\text{EW}(H\alpha) = 75 \pm 25$ Å. The shape of the distribution is very similar to that seen for the rest-frame $H\alpha$ EWs of local ULIRGs from Veilleux et al. (1999), which have a median $\text{EW}(H\alpha) = 73 \pm 8$ Å suggesting that the unobscured/partially observed mix of emission-line gas and stellar continuum is comparable to local ULIRGs (although we note that the projected size of the spectroscopy apertures in the local ULIRGs is less than 1 kpc, whereas for the SMGs/OFRGs the projected size is ~ 10 kpc; thus some caution should be taken when comparing the two samples).

Our SMG/OFRG sample is intrinsically luminous in the far-infrared, but their $H\alpha$ flux (and estimated SFR) is much less than expected with a median SFR($H\alpha$) compared to SFR(IR) of 94 ± 20 and $1380 \pm 190 M_{\odot} \text{yr}^{-1}$, respectively. Overall, the $H\alpha$ SFRs are suppressed by at least a factor of ten relative to that suggested by the far-infrared. In comparison to other far-infrared-selected samples, we see that the SMGs/OFRGs extend the trend for proportionally less $H\alpha$ luminosity in more far-infrared luminous galaxies. As we have shown there is no detectable difference between the far-infrared luminosities of the starburst- and AGN-classed galaxies in our sample – suggest-

ing that this declining ratio of $H\alpha$ to far-infrared emission is unlikely to be caused by an increasing AGN contribution. Hence, we attribute the variation to copious and increasing amounts of dust enshrouding the galaxy and extinguishing $H\alpha$ emission.

Unfortunately, the wavelength coverage of our spectroscopic observations does not extend to $H\beta$, and thus the reddening in these galaxies cannot be estimated directly from the Balmer decrement to confirm this suggestion, although attempts at estimating the reddening in this manner are underway for a subsample of galaxies. The only target with an $H\beta$ measurement in the literature is SMM J123707.21+621408.1 (Simpson et al. 2004), with an $H\beta$ flux of $2.1 \pm 0.9 \times 10^{-20} \text{ W m}^{-2}$. The $H\alpha/H\beta$ flux ratio is 8 ± 6 , which corresponds to a reddening of $A_V = 1.4 \pm 1.0$ (Calzetti et al. 1994); the large uncertainties arise from the modest signal-to-noise ratio detections of both $H\alpha$ and $H\beta$ emission lines. For the rest of the sample, we have attempted to derive the reddening for these galaxies from their broadband optical/near-infrared colours (Smail et al. 2004). These are derived by using the HYPER-Z photometric redshift code (Bolzonella et al. 2000) to fit young continuous star formation models with variable reddening and age to the galaxy photometry at their known redshifts. We find a median reddening of $A_V = 3.0 \pm 1.0$. Accounting for the contribution of $H\alpha$ to the K -band photometry may decrease this estimate slightly but the reddening estimated from the continuum colours indicates substantial extinction at the wavelength of $H\alpha$ (assuming that the continuum and line emission arise from the same regions in the galaxy). The scatter of a factor of 2.5 is more than sufficient to explain the dispersion in the strength of the $H\alpha$ emission at a fixed far-infrared luminosity. We conclude therefore that the large scatter in SFR(FIR)/SFR($H\alpha$) probably arises from two main factors: (1) there is a range in the continuum extinction in the more far-infrared luminous population and, (2) the morphological diversity of sub-mm-selected galaxies – which includes a large fraction of interacting or merging systems, sometimes with highly-obscured components may lead to a large variation in the in-slit $H\alpha$ fluxes for these systems (Chapman et al. 2003b; Smail et al. 2004).

2.11. Metallicities

Rest-frame optical emission lines from extra-galactic HII regions provide an important diagnostic of the chemical evolution of galaxies since their properties reflect the make-up of the (ISM). Moreover, feedback processes from short-lived massive stars in high SFR galaxies may be responsible for the enrichment of the intergalactic medium (IGM) with heavy metals over a wide range of redshifts (Heckman et al. 2000; Adelberger et al. 2003). For star-forming and irregular galaxies the correlation between metallicity (traced by Oxygen abundances, O/H) and rest-frame luminosity is well established in the local universe and spans a factor of over 100 in (O/H) and at least eight magnitudes in M_V . The correlation is in the sense that more massive (and luminous) galaxies exhibit a higher degree of metal enrichment (Garnett et al. 1987; Zaritsky et al. 1994; Garnett 2002; Lilly et al. 2003; Lamareille et al. 2004). If such a correlation exists at high redshift then it may be more important for understanding the present distribution of metals in the universe, since the bulk of the star-formation activity in the most massive and active galaxies is thought to occur at $z > 1$ (Blain et al. 1999b).

Since we lack the observations necessary to calculate the R_{23} index (Zaritsky et al. 1994) for our sample, we turn to the $N2$ index described by Storchi-Bergmann et al. (1994)

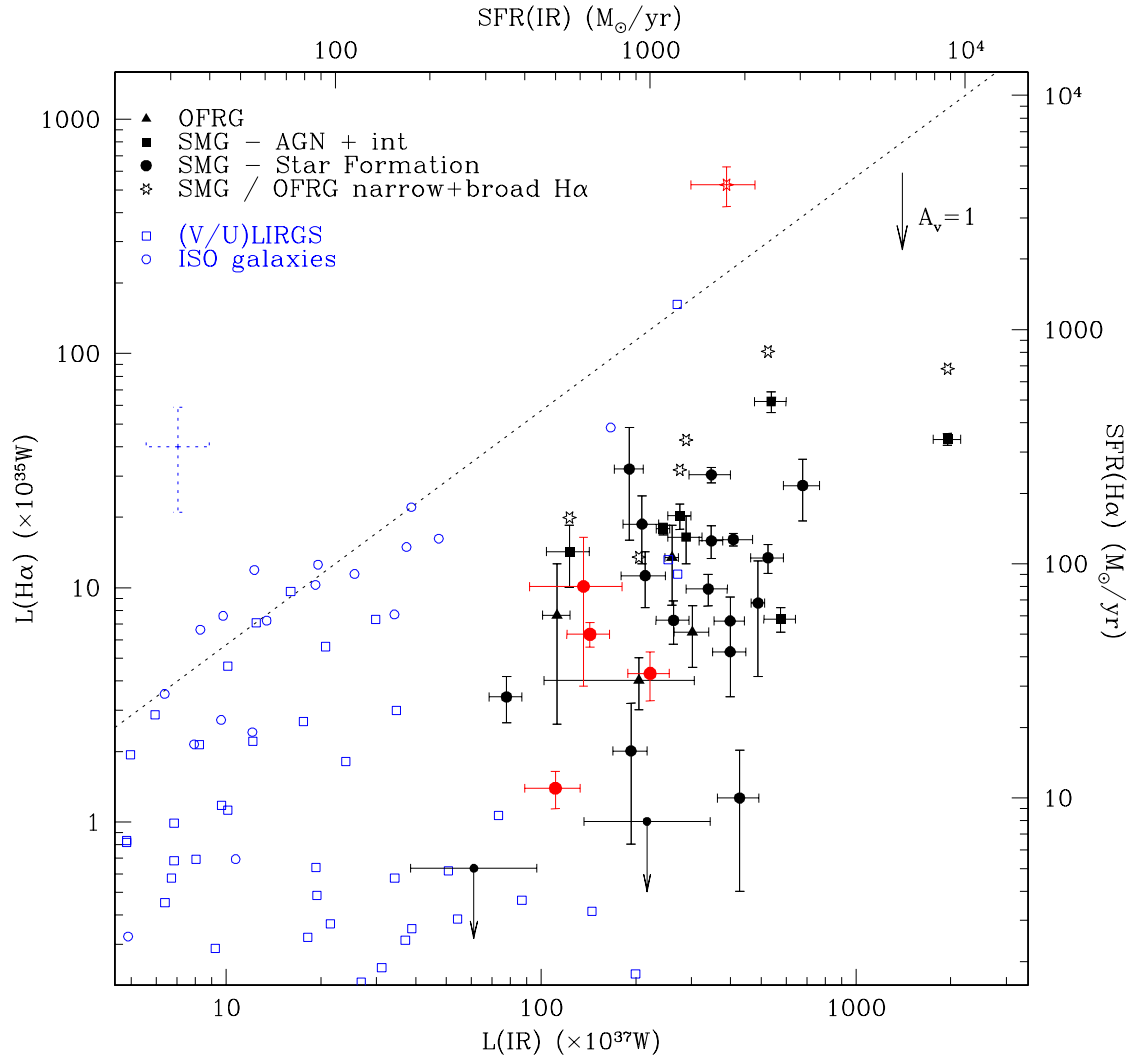


FIG. 8.— Comparison of the far-infrared vs. narrow-line $H\alpha$ luminosities and star formation rates in our data with those in local samples. We include in the plot the SFRs for the SMGs/OFRGs when the broad-line $H\alpha$ flux is included in the estimate (the galaxies classified as intermediate in §2.4 are included with the AGN classification). This is more comparable to the quantities calculated for local samples. We also include the previously published SMGs (Kneib et al. 2004; Dey et al. 1999; Smail et al. 2003; Frayer et al. 2003; Ivison et al. 1998) as red points ordered from lowest to highest $H\alpha$ luminosity respectively. The dotted line represents identical estimated SFR from $H\alpha$ and far-infrared. The sample is compared to the results from ISOCAM, including the $z = 0.2$ – 1.5 galaxies in the Hubble Deep Field-South by Franceschini et al. (2003) and the local luminous infra-red galaxy sample ($z = 0.2$ – 0.7) by Flores et al. (2004). We also compare the data to the Very Luminous and Ultra-Luminous infrared galaxy sample of local *IRAS* greater than 2Jy sources by Dopita et al. (2002) and Poggianti & Wu (2000). We include a representative error bar from the comparison samples on the left side of the plot.

and discussed more recently by Denicolo et al. (2002) and Pettini & Pagel (2004). This indicator is defined at $N2 = \log([\text{NII}]\lambda 6584/H\alpha)$ and is calibrated to the oxygen abundance (O/H) via $12 + \log(O/H) = 8.90 + 0.57 \times N2$ (Pettini & Pagel 2004). However, this calibration remains uncertain, and there are obvious drawbacks to using this index for young galaxies in which AGN may play a role in defining the emission-line characteristics and in which primary and secondary sources of Nitrogen production may lead to mismatches in N/O . For this reason we have chosen to compare populations directly using their $N2$ measurements (as opposed to O/H measured from a range of indicators) to minimise systematic uncertainties arising from the calibration from $N2$ to O/H . We therefore deter-

mine the $N2$ index for all of the galaxies in our sample and give upper limits where the $[\text{NII}]$ emission line is not detected with sufficient significance to measure accurately.

In Fig. 9 we show the distribution of M_V versus $N2$ for SMGs/OFRGs as a proxy for their Luminosity–Metallicity relation and compare this with similar observations of both local and high redshift galaxy populations. To calculate the observed rest-frame V -band luminosities of the SMGs we use the photometry from Smail et al. (2004) and fit SED’s based on their observed broad-band *IJK* magnitudes, which, at $z \sim 2.4$, corresponds to rest-frame *UBR*, bracketing the V -band. As Smail et al. (2004) show, the competing effects of dust reddening and fading of the young stellar populations almost cancel each other

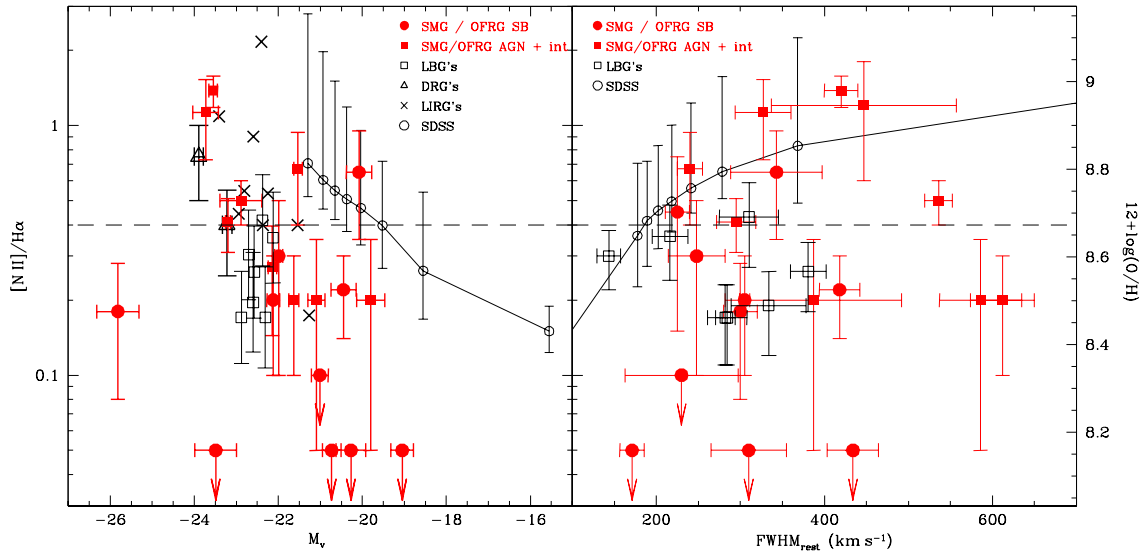


FIG. 9.— *Left*: Metallicity-Luminosity relation for SMGs/OFRGs. *Right*: Line width - metallicity relation for the SMGs/OFRGs. The abundance is derived using the $N2$ index calibration given by Pettini & Pagel (2004). We show two low-redshift samples for comparison, one from the SDSS DR2 (Abazajian et al. 2004) and one for local luminous infrared galaxies (Armus et al. 1989). For a higher redshift comparison sample, we show the metallicities for the $z \sim 2$ UV-selected galaxies from Shapley et al. (2004) and for a near-infrared-selected sample of luminous, $z \sim 2$ galaxies from van Dokkum et al. (2004). The horizontal dashed line represents solar metallicity. The SMGs/OFRGs exhibit a large range in M_V and $\text{FWHM}_{\text{rest}}$, and many have slightly sub-solar or solar abundances. Note that these are the observed V -band luminosities (uncorrected for reddening; c.f. Fig. 7).

($\Delta_{\text{dust}}V \sim 3-4$, $\Delta_{\text{fade}}V \sim 4$ based on fitting the broadband colors of this population). Thus, we expect that the present-day descendants of these galaxies would have absolute luminosities not very dissimilar to those we have estimated (see also Fig. 7). For the comparison samples we convert the rest-frame B -band magnitudes for the UV-selected $z \sim 2$ sample from Shapley et al. (2004) using their $(R-K)$ colors to predict the rest-frame V -band magnitudes. We also convert the median, 10 and 90 percentile trend lines from a volume-limited ($z < 0.1$) local emission-line galaxy sample from the SDSS DR2 (Abazajian et al. 2004; although we stress that the Sloan aperture only samples the central ~ 3 kpc of a galaxy at $z = 0.05$ whereas the NIRSPEC slit will sample ~ 10 kpc at $z = 2.3$). We see at least an order-of-magnitude range in $N2$ for the SMGs/OFRGs (discounting obvious AGN), with little correlation between the line index and rest-frame luminosity. The implied median metallicity is slightly below solar, and appears to be similar to that inferred for bright, UV-selected galaxies at $z \sim 2$ (Shapley et al. 2004).

To address the competing and uncertain effects of dust reddening and passive fading of the stellar populations on the M_V versus $[\text{NII}]/\text{H}\alpha$ plot, we have also constructed a $\text{FWHM}_{\text{H}\alpha}$ versus $[\text{NII}]/\text{H}\alpha$ diagram, adopting the $\text{FWHM}_{\text{H}\alpha}$ as a crude proxy for the dynamical mass of the galaxies. As can be seen, the large dynamical masses we inferred for the SMG/OFRG population suggest that their present-day descendants are likely to be luminous and metal-rich (super-solar) systems (as shown by the trends seen in the SDSS dataset plotted in Fig. 9). The apparently modest metallicities we measure would then indicate that these systems are seen during an early phase of enrichment – suggesting that they are relatively youthful galaxies and arguing against them undergoing a cycle of repeated short (~ 10 Myr) bursts of star-formation over a relatively extended period ($\gtrsim 1$ Gyr; Smail et al. 2003). However, there are other possible explanations for the apparently low metallicities of these galaxies. First, we note that star-formation can usually

only act to increase a galaxy’s metallicity (and therefore $N2$), and in particular starburst-driven feedback mechanisms are unlikely to preferentially expel large quantities of metals without entraining and expelling associated gas. Only an infall of unenriched material into the galaxy could cause the metallicity and effective heavy-element yield to decrease (e.g., Garnett 2002). Alternatively, if these systems are very young and the halos of the SMGs/OFRGs have yet to coalesce (as suggested by the clear merger/interacting morphologies of many systems), then the metallicities we measure may reflect those of the progenitor components. The similarity of the $N2$ estimates with those for the UV-selected population at this epoch could then be interpreted as indicating that the SMGs/OFRGs arise from mergers among the UV population. The slightly more evolved descendants of these mergers will be able to retain their enriched gas and so produce a super-solar stellar population. We stress that local calibrations of the $N2$ index from HII regions can show super-solar metallicities which may not reflect the global abundance in a galaxy. However, since our spectroscopic slit covers most of the area of our galaxies and the measured $\text{H}\alpha$ fluxes suggest substantial star-formation, we suggest that the $N2$ index should provide a fair estimate of the metallicity of the gas in the galaxy as a whole. We caution that the nitrogen abundances that we measure come from primary metal enrichment, whereas the local N/O versus O/H relations suggest that for metal-rich systems the nitrogen is secondary in origin (produced from intermediate mass stars far removed from the first generation). The evolution of the nitrogen metallicity–luminosity relation might be therefore quite different from that shown for oxygen or other α -elements. We also note that the $N2$ index is not an ideal metallicity indicator given the presence of an AGN in many of these galaxies, and we look forward to future studies based on $[\text{OII}]$, $[\text{OIII}]$ and $\text{H}\beta$ emission lines.

Using deep *Chandra* observations of the Hubble Deep Field (HDF), ELAIS N2 field, and SSA13 field (Alexander et al. 2003b; Manners et al. 2003; Mushotzky et al. 2000), it is possible to compare the X-ray and $H\alpha$ properties of the SMGs/OFRGs which overlap with the *Chandra* coverage. Of the 18 sources which were covered by *Chandra*, nine were detected in the 2–8 keV hard X-ray band, mostly in the HDF owing to the much deeper X-ray observations available for that field. We convert the observed 2–8 keV flux to a rest-frame 2–10 keV luminosity using $L_X = 4\pi d_L^2 f_X (1+z)^{\Gamma-2}$, which takes into account the k -correction (Alexander et al. 2003b), assuming a spectral index $\Gamma = 2$.

In Fig 10 we compare the $H\alpha$ luminosities from the SMGs/OFRGs to their X-ray luminosities and contrast these with a local sample of *IRAS*-selected Seyfert galaxies analysed by Ward et al. (1988). We also overlay two lines showing the correlation of $L_{(2-10\text{KeV})}$ versus $L(\text{FIR})$ from Ranalli et al. (2003). The first line simply converts their $L(\text{FIR})$ to $L(H\alpha)$ assuming that the relation in §2 holds, and the second line assumes a further 10 times suppression of the $H\alpha$ emission (relative to the far-infrared) as indicated by Fig. 8.

The distribution of the SMGs/OFRGs in Fig. 10 roughly follows that seen for the Ward et al. (1988) sample – *irrespective* of the spectral classification of the SMGs/OFRGs. However, we note that the correlation for local star-forming galaxies from Ranalli et al. (2003) – if scaled for the relative underluminosity of $H\alpha$ in the SMGs/OFRGs – can explain the properties of the least X-ray luminous galaxies, these comprise roughly half of our sample.

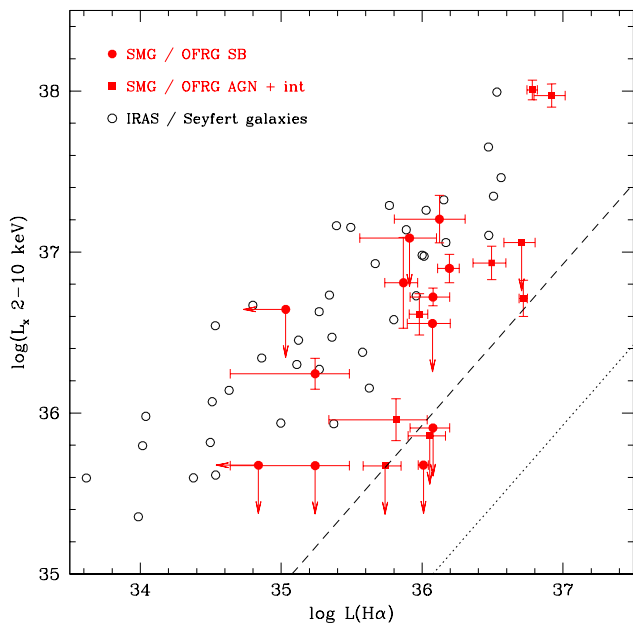


FIG. 10. – Distribution of $H\alpha$ and X-ray luminosities for the SMGs/OFRGs in our sample as compared to the local *IRAS*-selected Seyfert galaxies from Ward et al. (1988). For the SMGs/OFRGs sample we plot the total $H\alpha$ luminosity from both narrow and broad components (if present). We also compare the data to a sample of nearby star-forming galaxies by Ranalli et al. (2003), shown by a dotted line (converting their $L(\text{FIR})$ to $L(H\alpha)$ assuming the correlation in §2 holds) and include the same line but assuming a 10 times suppression of the $H\alpha$ emission (relative to the far-infrared) as indicated in Fig. 8, shown by a dashed line. The plot shows that some SMGs/OFRGs which are identified as star-forming in the near-infrared (with $\text{FWHM} \leq 500 \text{ km s}^{-1}$ and $[\text{NII}]/H\alpha \lesssim 0.7$)

show 2–10 keV X-ray fluxes consistent with AGN luminosities. It is also interesting to note that some of the SMGs/OFRGs which are spectroscopically-classified as AGN from their near-infrared spectra are not detected in the hard X-ray band.

The most intriguing galaxies in Fig. 10 are those which have high X-ray luminosities ($\log L_x \gtrsim 36.5$) but have restframe optical spectral classifications of star-formation – the X-ray luminosity in these galaxies probably arises from an AGN which is so highly obscured that either it is hidden in the rest-frame optical spectra (given their modest signal to noise) or we missed the AGN component with our spectroscopic slit in these systems. The presence of a broad-line component in the composite star-forming spectrum in §3.2 would support the former interpretation.

We also point out that there are six SMGs/OFRGs which are not detected to a flux limit of $1.4 \times 10^{-19} \text{ W m}^{-2}$ in the 2-Ms *Chandra* observations of the HDF (two) or $2.2 \times 10^{-18} \text{ W m}^{-2}$ in the ELAIS N2 (four) field. While three of these are classified as SB from their restframe optical spectra, three others show some signs of AGN in the near-infrared spectra (with broad $H\alpha$ or large $[\text{NII}]/H\alpha$ ratios). The X-ray limits on two of these (SMMJ163650.43 and SMMJ163706.51) are particularly stringent – yet they show clear AGN signatures in their near-infrared spectra. The detection of broad $H\alpha$ and lack of X-ray emission are difficult to understand – with these galaxies being almost an order of magnitude fainter in the X-ray waveband than expected from their $H\alpha$ luminosities. Given the amount of gas available to fuel an AGN in these systems, we conclude that they are likely to be intrinsically low luminosity and probably have low mass central black holes.

3. CONCLUSIONS

We present the results of near-infrared spectroscopic and narrow-band detections or limits on the $H\alpha$ emission from a sample of 30 ultraluminous, dusty galaxies at $z \sim 1.4\text{--}2.7$. The majority of these galaxies come from sub-mm/mm-surveys, with a small number identified as probable hot, luminous far-infrared sources from their radio emission. We see no difference between the properties of these two samples in any of our diagnostic diagrams – supporting the claimed similarity of the two populations (Chapman et al. 2004b).

We identify the $H\alpha$ emission in the near-infrared spectra and use the spectra to classify AGN by flagging galaxies with large $[\text{NII}]/H\alpha$ ratios (≥ 0.7) and/or large $H\alpha$ FWHM ($> 500 \text{ km s}^{-1}$). We find that the ratio of AGN- to star formation- dominated galaxies from the rest-frame optical spectroscopy is roughly 40%:60% – similar to the proportions estimated from their UV spectra by Chapman et al. (2003a, 2003b, 2004c). By constructing a rest-frame composite spectrum for the entire sample, we find that average $[\text{NII}]/H\alpha$ ratio is 0.42 ± 0.05 , which suggests that the composite is star-formation- rather than AGN-dominated, although it has an underlying broad-line component. Furthermore the composite spectra show both NaD absorption and $[\text{SII}]$ emission features, although we find no evidence of velocity offsets between these features and the $H\alpha$ emission. The $[\text{SII}]/H\alpha$ emission ratio in the composite spectrum is 0.10 ± 0.04 – indicating that the spectral properties of our sample are comparable to a LINER or HII region – similar results are found from the spectral classifications of local ULIRGs (Veilleux et al. 1987, 1995).

We also derive the composite spectrum for those galaxies which, individually, show no signs of an AGN in their near-

infrared spectra. This composite has an average $[\text{NII}]/\text{H}\alpha$ flux ratio of 0.19 ± 0.05 and $\text{FWHM}_{\text{rest}}$ of $400 \pm 70 \text{ km s}^{-1}$. However, the most striking result is that the composite spectrum appears to show an underlying broad $\text{H}\alpha$ line with a broad/narrow $\text{H}\alpha$ flux ratio of 0.45 ± 0.20 , suggesting that even these galaxies may host a low-luminosity AGN which is undetectable in our modest signal-to-noise spectroscopy.

In seven of the systems with spectroscopic observations we find velocity structure in the $\text{H}\alpha$ emission line. By comparison with high-resolution broadband imaging, we identify these galaxies as multi-component (probably interacting) systems with typical velocity offsets between components of $100\text{--}600 \text{ km s}^{-1}$. This is not surprising since locally many far-infrared luminous galaxies appear to be disturbed/interacting systems. Assuming that these are merging systems with random orientations of their orbits on the sky, we estimate a typical mass of $1.5 \pm 0.9 \times 10^{11} M_{\odot}$. We obtain a similar estimate from the $\text{H}\alpha$ line widths of the whole sample. These estimates are comparable to the dynamical mass estimates from CO observations of a subset of these systems.

In all of the galaxies, we have attempted to deconvolve any broad component to the $\text{H}\alpha$ line (which comes from an accretion disk around a central super-massive black hole) from the narrow-line $\text{H}\alpha$ flux (which comes from the star-forming regions). Using the narrow-line $\text{H}\alpha$ flux, we compare the SFRs of the SMGs/OFRGs as compared to the SFR derived from the far-infrared emission. The $\text{SFR}(\text{H}\alpha)$ versus $\text{SFR}(\text{FIR})$ correlation shows a large scatter, with the $\text{SFR}(\text{H}\alpha)$ typically a factor of ten less than what we would expect from their far-infrared luminosities. Most of this scatter, however, can be explained by the reddening in these systems (estimated from their broad-band photometry in Smail et al. (2004)). The suppression of the $\text{H}\alpha$ flux is therefore attributed to both heavily obscured galaxies and a diverse range of morphologies. The average SFR derived from $\text{H}\alpha$ for the SMGs/OFRGs in our sample is $94 \pm 20 M_{\odot} \text{ yr}^{-1}$ (uncorrected for extinction). Since the continuum extinction correction at 6563 \AA is ~ 2.5 magnitudes, the total inferred SFR of these galaxies is expected to be $\sim 1000 M_{\odot} \text{ yr}^{-1}$ – comparable to that seen in the far-infrared. We also compare the SFR properties for our high-redshift sample to local Very/Ultra-Luminous galaxy samples and find that the scatter within our high redshift SMGs/OFRGs and the distribution of equivalent widths are comparable to those of local Ultra/Very luminous galaxy samples. This suggests a similar range of obscured/unobscured activity in the distant population to that seen locally, although with a higher proportion of the star formation completely obscured from view.

Using the $N2$ index, we have investigated the chemical abundances of these galaxies and find that the $N2$ indices for the SMGs/OFRGs suggest that they have slightly sub-solar metallicities, similar to recent results from UV selected galaxies at these early epochs (Shapley et al. 2004). However, we note that the $N2$ indicator may not be a reliable metallicity indicator for this population – especially in the presence of an AGN. We find that the SMGs/OFRGs in our sample display a large range in $[\text{NII}]/\text{H}\alpha$ versus M_V or $\text{FWHM}_{\text{rest}}$ (which we use as a proxy for their dynamical masses).

For the galaxies which are in the HDF, ELAIS N2 field and SSA13 field we use their X-ray properties in order to further classify the galaxies. The SMGs/OFRGs classified as AGN on the basis of their near-infrared spectra broadly follow the correlation seen between X-ray and $\text{H}\alpha$ luminosities for local

Seyfert 2 galaxies (Ward et al. 1988). We find that a subset of galaxies which are spectroscopically-classified as star-forming in the near-infrared have high X-ray luminosities, suggesting that they host highly obscured AGN. Likewise, a small number of near-infrared spectroscopically-classified AGN are undetected in deep *Chandra* observations. We conclude that these galaxies are likely to be intrinsically low luminosity and probably have low-mass central black holes.

With observations of the $\text{H}\alpha$ emission from these SMGs/OFRGs at $z \sim 2$ we can at last start to directly compare these galaxies to similarly distant UV-selected systems. We find that as expected the $\text{SFR}(\text{H}\alpha)$ for our sample is nearly an order of magnitude higher than that found in $z \sim 2$ UV-selected galaxies by Erb et al. (2003) (who find an average $\text{SFR}(\text{H}\alpha)$ of $21 \pm 3 M_{\odot} \text{ yr}^{-1}$ – even after their sample is corrected for extinction). Similarly, the line widths and dynamical information suggest that the halos of a typical SMG/OFRGs may be up to 5 times more massive than the UV-selected population. We also find a higher rate of AGN activity in the SMG/OFRGs – suggesting the presence of actively fueled and growing super-massive black holes in these galaxies. However, somewhat surprisingly, we find similar metallicities for the UV-selected and more massive far-infrared luminous populations. We suggest that this may be explained if the SMG/OFRGs are relatively youthful, with their deepening potential wells not yet sufficiently organised to retain a larger fraction of the enriched material from their star formation activity.

Overall our observations suggest that the high redshift SMG/OFRG population shares many of the characteristics of similar (but somewhat less luminous) far-infrared galaxies identified in the local Universe. This includes the $\text{H}\alpha$ equivalent widths, the proportion of obvious AGN and the typical optical spectral classification. Previous work has demonstrated the preponderance of merger-like morphologies in the two populations and the similarity of their restframe optical luminosities. Yet there remain differences, with proportionally more highly-obscured activity in the high-redshift population, apparently larger dynamical mass, lower metallicities and higher gas fractions on 10-kpc scales.

We conclude that the SMG/OFRGs in our sample represent a population of young, massive merging/interacting systems, the results of which cause high instantaneous bursts of (highly obscured) star-formation and actively fueled AGN activity. Although these bursts are brief, they can form all of the stars in an L^* galaxy and in doing so will raise the metallicity of these systems closer to that required by observations of their likely present-day descendants: luminous elliptical galaxies.

We thank the referee for his constructive comments and suggestions which significantly improved the content of this paper. We would like to thank David Gilbank for adapting I-PIPE and extensive help reducing the IRTF narrow-band imaging and Mike Balogh, Chris Miller and Bob Nichol for providing the SDSS catalogs in a usable format. We acknowledge useful conversations or help from Dave Alexander, Carlton Baugh, Richard Bower, Chris Done, Dave Gilbank, Cedric Lacey, Max Pettini, Alice Shapley, Chris Simpson, Kaz Sekiguchi, Tadamuni Takata and Richard Whitaker. AMS acknowledges support from PPARC, IRS acknowledges support from the Royal Society. AWB acknowledges support from NSF AST-0205937 and the Alfred Sloan Foundation.

REFERENCES

- Abazajian, K. et al. (The SDSS Collaboration) 2004, AJ, submitted
- Adelberger, K. L., Steidel, C. C., Shapley, A. E., & Pettini, M., 2003, ApJ, 584 45
- Alexander, D. M., Bauer, F. E., Brandt, W. N., Hornschemeier, A. E., Vignali, C., Garmire, G. P., Schneider, D. P., Chartas, G., & Gallagher, S. C., 2003a, AJ, 125 383
- Alexander, D. M., Bauer, F. E., Brandt, W. N., Schneider, D. P., Hornschemeier, A. E., Vignali, C., Barger, A. J., Broos, P. S., Cowie, L. L., Garmire, G. P., Townsley, L. K., Bautz, M. W., Chartas, G., Sargent, W. L. W., 2003b, AJ 126 539
- Armus, L., Heckman, T. M., & Miley, G. K. 1989, ApJ 347 727
- Barger, A. J., Cowie, L. L., Smail, I., Ivison, R. J., Blain, A. W., & Kneib, J.-P. 1999, AJ, 117 2656
- Baugh, C. M., Lacey, C. G., Frenk, C. S., Granato, G. L., Silva, L., Bressan, A., Benson, A. J., & Cole, S., 2004 MNRAS submitted
- Blain, A. W., Chapman, S. C., Smail, I., & Ivison, R. J., 2004, ApJ in press
- Blain, A. W., Kneib, J.-P., Ivison, R. J., & Smail, I. 1999a, ApJ, 512 87
- Blain, A. W., Smail, I., Ivison, R. J., & Kneib, J.-P., 1999b, MNRAS, 302 632
- Bolzonella, M., Miralles, J.-M., & Pelló, R. 2000, A&A, 363 476
- Bryant, P. M. & Scoville, N. Z. 1996, ApJ, 457 678
- Calzetti, D., Kinney, A. L., Storchi-Bergmann, T., 1994 ApJ 429 582
- Chapman, S. C., Richards, E. A., Lewis, G. F., Wilson, G., & Barger, A. J., 2001, ApJ, 548L 147
- Chapman, S. C., Windhorst, R., Odewahn, S., Yan, H., & Conselice, C. 2003a, ApJ, 599 92
- Chapman, S. C., Blain, A. W., Ivison, R. J., & Smail, I., 2003b, Nature, 422 695
- Chapman, S. C., Blain, A. W., Smail, I., & Ivison, R. J., 2004a, ApJ, submitted
- Chapman, S. C., Smail, I., Blain, A. W., & Ivison, R. J., 2004b, ApJ, submitted
- Chapman, S. C., Smail, I., Blain, A. W., & Ivison, R. J., 2004c, ApJ, submitted
- Condon, J. J., Anderson, M. L., & Helou, G. 1991, ApJ, 376 95
- Cowie, L. L., Barger, A. J., & Kneib, J. P. 2002, AJ, 123 2197
- Dawson, S., McCrady, N., Stern, D., Eckart, M. E., Spinrad, H., Liu, M. C.; Graham, J. R. 2003 AJ, 125 1236
- Denicolo, G., Terlevich, R., & Terlevich, E., 2002, MNRAS, 330 69
- Dey, A., Graham, J. R., Ivison, R. J., Smail, I., & Wright, G. S., & Liu, M. C. 1999, ApJ, 519 610
- Dopita, M. A., Pereira, M., Kewley, L. J., & Capaccioni, M. 2002, ApJS, 143 47
- Downes, D. & Solomon, P. M. 2003, ApJ, 582 37
- Erb, D. K., Shapley, A. E., Steidel, C. C., Pettini, M., Adelberger, K. L., Hunt, M. P., Moorwood, A. F. M., & Cuby, J. 2003, ApJ, 591 101
- Faber, S. M., & Jackson, R. E., 1976, ApJ, 204 668
- Ferland, G. J., & Osterbrock, D. E. 1986 ApJ, 300 658
- Flores, H., Hammer, F., Elbaz, D., Cesarsky, C. J., Liang, Y. C., Fadda, D., & Gruel, N. 2004, A&A, 415 885
- Franceschini, A., Berta, S., Rigopoulou, D., Aussel, H., Cesarsky, C. J., Elbaz, D., Genzel, R., Moy, E., Oliver, S., Rowan-Robinson, M., & Van der Werf, P. P. 2003, A&A, 403 501
- Frayser, D. T., Armus, L., Scoville, N. Z., Blain, A. W., Reddy, N. A., Ivison, R. J., & Smail, I. 2003, AJ, 126 73
- Frayser, D. T., Ivison, R. J., Scoville, N. Z., Evans, A. S., Yun, M. S., Smail, I., Barger, A. J., Blain, A. W., & Kneib, J.-P. 1999, ApJ, 514 L13
- Garnett, M. A. Shields, G. A., Skillman, E. D., Sagan, S. P., & Dufour, R. J., 1997, ApJ, 489 63
- Garrett, M. A. 2002, A&A, 384 L19
- Genzel, R., Baker, A. J.; Tacconi, L. J., Lutz, D., Cox, P., Guilleoteau, S., & Omont, A., 2003 ApJ 584 633
- Giavalisco, M. et al. 2004, ApJ, 600 93
- Greve, T. R., et al. 2004 in prep.
- Hawarden, T. G., Leggett, S. K., Letawsky, M. B., Ballantyne, D. R., & Casali, M. M. 2001, MNRAS, 325 563
- Heckman, T. M., Lehnert, M. D., Strickland, D. K., & Armus, L. 2000, ApJS, 129 493
- Ivison, R. J., Smail, I., Le Borgne, J.-F., Blain, A. W., Kneib, J.-P., Bezecourt, J., Kerr, T. H., & Davies, J. K. 1998, MNRAS, 298 583
- Ivison, R., Smail, I., Blain, A., Kneib, J., & Frayer, D. 1999, Ap&SS, 266 285
- Ivison, R. J., Smail, I., Barger, A. J., Kneib, J.-P., Blain, A. W., Owen, F. N., Kerr, T. H., & Cowie, L. L. 2000, MNRAS, 315 209
- Ivison, R. J., Smail, I., Frayer, D. T., Kneib, J.-P., & Blain, A. W. 2001, ApJ, 561 L45
- Ivison, R. J., Greve, T. R., Smail, I., Dunlop, J. S., Roche, N. D., Scott, S. E., Page, M. J. Stevens, J. A., Almaini, O., Blain, A. W., Willott, C. J., Fox, M. J., Gilbank, D. G., Serjeant, & S. Hughes, D. H., 2002, MNRAS, 337 1
- Jørgensen, I., Franx, M., Hjorth, J., van Dokkum, P.G., 1999, MNRAS, 308 833
- Jørgensen, I., Franx, M., Kjærgaard, P., 1995a, MNRAS, 273 1097
- Jørgensen, I., Franx, M., Kjærgaard, P., 1995a, MNRAS, 276 1341
- Kennicutt, R. C. 1998, ARA&A, 36 189
- Kneib, J., van der Werf, P. P., Kraiberg Knudsen, K., Smail, I., Blain, A., Frayer, D., Barnard, V., & Ivison, R., 2004, MNRAS, 349 1211
- Lamareille, F., Mouhcine, M., Contini, T., Lewis, I., & Maddox, S. 2004, MNRAS, 350 396
- Lilly, S. J., Eales, S. A., Gear, W. K. P., Hammer, F., Le Fevre, O., Crampton, D., Bond, J. R., & Dunne, L., 1999, ApJ, 518 641
- Lilly, S. J., Marcella Carollo, C., Stockton, A. N., AJ, 597 730
- Leitherer, C. & Heckman, T. M. 1995, ApJS, 96, 9
- Lutz, D., Veilleux, S., & Genzel, R., 1999, ApJ 517, 13
- McLean, I. S., Becklin, E. E.; Bendiksen, O., Brims, G., Canfield, J., Figer, D. F., Graham, J. R., Hare, J., Lacayanga, F., & Larkin, J. E. 1998 SPIE 3354 566
- Moorwood, A. F. 1997, SPIE, 2871 1146
- Neri, R., Genzel, R., Ivison, R. J., Bertoldi, F., Blain, A. W., Chapman, S. C., Cox, P., Greve, T. R., Omont, A., & Frayer, D. T. 2003, ApJ, 597 L113
- Pettini, M., Shapley, A. E., Steidel, C. C., Cuby, J., Dickinson, M., Moorwood, A. F. M., Adelberger, K. L., & Giavalisco, M., 2001, ApJ, 554 981
- Pettini, M., & Pagel, B. E. J. 2004, MNRAS, 348 59
- Phillips, A. C. 1993, AJ, 105 486
- Poggianti, B. M. & Wu, H. 2000, ApJ, 529 157
- Ranalli, P., Comastri, A., Setti, G., 2003, A&A, 399 39
- Roche, P. F., Lucas, P. W., Mackay, C. D., Etedgui-Atad, E., Hastings, P. R.; Bridger, A., Rees, N. P., Leggett, S. K., Davis, C., Holmes, A. R., & Handford, T. 2003 SPIE 4841 901
- Rupke, D. S., Veilleux, S., & Sanders, D. B. 2002, ApJ, 570 588
- Simpson C. et al. 2004, MNRAS, in press.
- Shapley, A. E., Erb, D. K., Pettini, M., Steidel, C. C., & Adelberger, K. L., 2004, ApJ, in press
- Shure, M., Toomey, D. W., Rayner, J., Onaka, P., Denault, A., Stahlberger, W., Watanabe, D., Criez, K., Robertson, L., & Cook, D. 1993 AAS 183 11701
- Smail, I., Ivison, R. J., Blain, A. W., & Kneib, J. P. 2002 MNRAS, 331 495
- Smail, I., Ivison, R. J., Gilbank, D. G., Dunlop, J. S., Keel, W. C., Motohara, K., & Stevens, J. A. 2003, ApJ, 583 551
- Smail, I., Chapman, S. C., Ivison, R. J., & Blain, A. W., 2004, ApJ in press
- Storchi-Bergmann, T., Calzetti, D., & Kinney, A. L. 1994, ApJ, 429 572
- Swinbank, A. M., Smail, I., Bower, R. G., Borys, C., Chapman, S. C., Blain, A. W., Ivison, R. J., Ramsey Howat, S., Keel, W., 2005 MNRAS in prep.
- Tecza, M., Baker, A. J., Davies, R. I., Genzel, R., Lehnert, M. D., Eisenhauer, F., Lutz, D., Nesvadba, N., Seitz, S., Tacconi, L. J., Thatte, N. A., Abuter, R., & Bender, R. 2004, ApJ, 605 L109
- Tully, R. B., Fisher, J. R. 1977A&A 54 661
- van Dokkum, P., Franx M., Schreiber, N. F., Illingworth, G., Daddi, E., Knudsen, K. K., Labbe, I., Moorwood, A., Rix, H. W., Rottgering, H., Rudnick, G., Trujillo, I., van der Werf, P., van der Wel, A., van Starckenburg, L., & Wuyts S., 2004, ApJ, submitted
- Veilleux, S., & Osterbrock, D. E 1987, ApJS, 63 295
- Veilleux, S., Kim, D.-C., Sanders, D. B., Mazzarella, J. M., & Soifer, B. T. 1995, ApJS, 98 171
- Veilleux, S., Kim, D.-C., & Sanders, D. B., 1999, ApJ, 522 113
- Wang, W. H., Cowie, L. L., Barger, A. J., ApJ in press
- Yan, L., McCarthy, P. J., Freudling, W., Teplitz, H. I., Malumuth, E. M., Weymann, R. J., & Malkan, M. A. 1999, ApJ, 519 L47
- Zaritsky, D., Kennicutt, Robert C., Jr., & Huchra, J. P. 1994, ApJ, 420 87